1   Revision 1

2

Evidence for post-depositional diffusional loss of hydrogen in quartz

phenocryst fragments within ignimbrites

5

6   Tamás Biró[1], István János Kovács[2*], Dávid Karátson[1], Roland Stalder[3], Edit Király[2], György

7   Falus[2], Tamás Fancsik[2], Judit K. Sándorné[4]

8   [1]Eötvös University, Institute of Geography and Earth Sciences, Department of Physical

9   Geography, Pázmány Péter sétány 1/C, H-1117, Budapest, Hungary

10   [2]Geological and Geophysical Institute of Hungary, Geochemical and Laboratory Department,

11   Stefánia út 14, H-1143, Budapest, Hungary

12   [3]University of Innsbruck, Institute of Mineralogy and Petrography, Innrain 52f, 6020, Innsbruck,

13   Austria

14   [4]Hungarian Institute for Forensic Sciences, Mosonyi u. 9, H-1087, Budapest, Hungary

15

16   * Corresponding author. Tel.: +36 20 550 69 35

17   e-mail address: kovacs.istvan.janos@mfgi.hu

18

19

20   **Abstract**

21   Ignimbrite-hosted quartz phenocryst fragments contain much lower hydroxyl defect

22   concentration than quartz in igneous rocks. Pre-eruptive and post-depositional loss of hydrogen

23   were hypothesized as the main processes for lowering the initial magmatic concentrations of

24   hydroxyl defects. The aim of this study was to examine the hydroxyl defect concentration of

25   quartz phenocryst fragments from various vertical positions above the base of pyroclastic density

26   current (PDC) deposits. It aims to record the vertical variations of hydroxyl defect concentrations

27   to have an insight into potential post-depositional hydrogen loss of PDC deposits. Ignimbrite-

28   hosted quartz phenocryst fragments were examined from two different ignimbrites in the Bükk

29   Foreland Volcanic Area (North Hungary). Unpolarized micro-FTIR measurements on 23-35

30   unoriented crystal fragments from each sample were performed representing 4 different vertical

31   positions of each site. Present results imply that hydroxyl defect concentrations show a

32   pronounced decrease upwards from the base of the deposits. The initial ~12 ppm hydroxyl defect

33   concentration decreases to <3 ppm within <10 meters from the base. Ignimbrites with contrasting

34   degree of welding are characterized by different hydroxyl defect concentrations of quartz

35   phenocryst fragments at the same height above the base. Thus, post-depositional dehydration is

36   supposed to be the main factor causing the observed vertical decreasing trend. The modelling of

37   post-depositional dehydration by considering typical ignimbrite emplacement temperatures (300 -

38   700°C) and thicknesses (20 - 50 m) revealed, that the different cooling rates and average crystal

39   diameters only could not cause the observed decrease in hydroxyl defect concentrations in

40   ignimbrites. Other factors, such as contrasting pre-depositional thermal history, presence of melt-

41   and fluid inclusion and crack density of crystals could also play an important role in affecting the

42   final hydroxyl defect concentrations.

43

44

45   **Keywords**: quartz, FTIR spectrometry, water, ignimbrites, diffusion

46

47

Introduction

48

49 Quartz is the second most abundant mineral in the continental crust after feldspar and is an

50 abundant phase in Si-oversaturated magmatic systems. Its structure allows the incorporation of

51 several trace elements via various substitutions: i) isovalent substitution of Ti^{4+} or Ge^{4+} for Si^{4+};

52 ii) coupled substitution of $P^{5+} + M^{3+} \rightarrow 2Si^{4+}$; iii) heteroelectronic $M^{3+} + M^{+} \rightarrow Si^{4+}$ substitutions;

53 iv) hydrogarnet substitution as $4H^{+} \rightarrow Si^{4+}$, where M^{+} and M^{3+} are mono- and a trivalent cations;

54 Götze et al. 2001, 2004; Müller et al. 2002, 2003; Stalder and Konzett 2012, Baron et al. 2015,

55 Frigo et al. 2016). The most abundant impurities are the $Al^{3+} + M^{+} \rightarrow Si^{4+}$ heteroelectronic

56 substitutions, where alkalis, such as Na^{+}, K^{+}, Li^{+} or commonly H^{+} have to be involved as charge

57 compensating monovalent cations (Götze et al. 2001; 2004). In this way H^{+} is incorporated as

58 hydroxyl defects (OH^{-}) directly bonded to the silica framework. Hydrogen could also be present

59 in quartz crystals as molecular water (H_2O) in nanoinclusions (Stenina 2004) and fluid micro-

60 inclusions that represent on average by far the most abundant water species in quartz (Aines et al.

61 1984; Stalder and Neuser 2013).

62 Studying trace element concentrations of quartz in igneous and volcanic rocks to get information

63 on petrogenetic conditions has become important recently. The titanium concentration of quartz

64 may be used as a geothermometer (Wark and Watson, 2006; Huang and Audétat 2012) and

65 allows outlining pre-eruptive thermal histories within the magma chamber (e.g., Shane et al.

66 2008; Campbell et al. 2009; Matthews et al. 2012). Hydroxyl defect concentrations of quartz are

67 also considered for petrogenetic investigations. The aluminum-related hydroxyl defect

68 concentration and the concentration of hydrogarnet substitutions were proposed as good

69 indicators of pressure during crystallization (Stalder and Konzett 2012; Baron et al. 2015). The

70 amount of Al-related hydroxyl defects in quartz phenocrysts from experimental runs from the

71 Qz–Ab–H_2O and granite–H_2O systems (at 5 and 25 kbar) ranged from ~40 to ~80 ppm H_2O by

3

72   wt. (hereafter referred to as 'ppm' for short), and from ~100 to ~140 ppm respectively and

73   showed a negative pressure-dependence (Stalder and Konzett 2012). On the other hand

74   hydrogarnet substitution was positively correlated with pressure (Stalder and Konzett 2012;

75   Baron et al. 2015).

76   From a petrological point of view among olivine, pyroxene and feldspars quartz has a potential

77   importance in volcanic systems, because it may record conditions just prior to eruptions (Charlier

78   et al. 2012; Kilgour et al. 2014; Hartley et al. 2014, Weis et al. 2015, 2016). Hydroxyl defects in

79   quartz are characterized by $>6 \times 10^{-13}$ m^2/s diffusional speed at temperatures higher than 700°C

80   (Kats 1962; Kronenberg et al 1986), thus hydroxyl defects are supposed to be sensitive to

81   changes in pre-eruptive P, T or chemical activities. In spite of this, there are only sporadic data on

82   the hydroxyl defect concentration in quartz crystals from volcanic systems. The first

83   measurements of hydroxyl defect concentrations in ignimbrite-hosted quartz phenocryst

84   fragments reported hydroxyl defect concentrations ranging from ~2.0 to ~4.1 ppm (Biró et al.

85   2016), which is much lower than those in experimental quartz: 40 - 80 ppm from Qz–Ab–H$_2$O

86   and 100 - 140 ppm from granite–H$_2$O systems or 6-12 ppm in quartz from plutonic rocks (Müller

87   and Koch-Müller 2009; Stalder and Konzett 2012). Both syn- and post-eruptive processes are

88   proposed as important factors causing these low concentrations (Biró et al. 2016). The diffusional

89   loss of hydrogen during the eruption and after deposition is supposed to play the major role in

90   lowering the 'original' hydroxyl defect concentrations.

91   In this study measurements on hydroxyl defect concentrations within ignimbrite-hosted quartz

92   phenocryst fragments were performed to probe the effect of post-depositional cooling on

93   hydroxyl defect concentrations. For this purpose various vertical levels above the base of two

94   ignimbrite deposits were considered.

95

4

96

Geological background, volcanology

98   We investigated two ignimbrite deposits, which are located in the Bükk Foreland Volcanic Area

99   in North Hungary (Fig. 1 a, Table 1). During the Tertiary – between 21 and 12 Ma – a

100   widespread Si-rich explosive volcanism took place in the Carpathian-Pannonian Region (Fig. 1 a;

101   Szabó et al. 1992; Pécskay et al. 2006). The extent, volume and source vents of the resulting fall

102   and pyroclastic density current – hereafter PDC – deposits are poorly constrained, because most

103   of the volcanic rocks have been buried by thick Quaternary sediments due to basin subsidence.

104   However, a representative part of the volcanic succession crops out at the Bükk Foreland

105   Volcanic Area in a ca. 40x10 km large area (Fig. 1 b), where volcanic products were deposited

106   during a 7.5 My interval from 21 to 13.5 Ma and exceeds ~700 m in thickness (Szakács et al.

107   1998; Pelikán 2005). Most of the deposits are thick subaerial ignimbrites displaying massive

108   lapilli tuff facies. Three main successions, as Lower-, Middle-, and Upper Ignimbrites were

109   distinguished via physical volcanological properties (Varga 1981; Capaccioni et al. 1995;

110   Szakács et al. 1998; Lukács et al. 2010), paleomagnetic rotations (Márton 1990; Márton and

111   Pécskay 1998; Márton et al. 2007), K/Ar age determinations (Márton and Pécskay 1998; Lukács

112   et al. 2007, 2010), major and trace element compositions of minerals (Lukács et al. 2007) and

113   matrix glass shards (Harangi 2005; Harangi and Lukács 2009; Lukács et al. 2009) and

114   composition of quartz- and feldspar-hosted silicate melt inclusions (Lukács et al. 2002, 2005).

115   We sampled two different ignimbrites: Eger and Bogács (Fig. 2). In summary, the investigated

116   succession at Eger shows a typical architecture of subaerial ignimbrites, deposited from the

117   collapse of a Plinian eruption column. It starts with a well-sorted Plinian fall deposits and after

118   that a cross-bedded, fine-grained and finally a thick, massive lapilli tuff from a PDC follows.

119   This succession is a non-welded ignimbrite. At Bogács, the investigated ignimbrite is a slightly

120 welded PDC deposit, without initial Plinian fall deposit. At the latter site, only the lowermost,

121 ground-hugging 0.2 m is non-welded.

122 At Eger, samples from a typical, non-welded subaerial ignimbrite were collected which belongs

123 to the Lower Ignimbrite Unit. This deposit overlies the Oligocene sediments, thus known to be

124 one of the first products of the widespread intrabasinal Si-rich volcanism in the Carpathian-

125 Pannonian Region (Capaccioni et al. 1995; Szakács et al. 1998). Potassium/argon age

126 determinations resulted 20.2±1.7 and 19.7±0.9 Ma (Márton and Pécskay 1998). At Eger the

127 succession begins with a 0.2 m thick, very well-sorted, coarse tuff (Fig. 2). The layer has a

128 constant thickness irrespective the paleotopography. Pumice fragments have maximum and

129 average diameters of 2 and 0.5 cm, respectively. The lithics and crystals are smaller ~ 0.5 cm in

130 diameter. Internal structure or bedding is not visible. On the basis of its sedimentological

131 features, this layer is considered as a fall deposit (Capaccioni et al. 1995). The second layer is a

132 very fine-grained, cross bedded fine ash tuff with 0.2 m in thickness, which cover the fall deposit

133 with a sharp contact. Pumice fragments are rare and are 1 - 2 mm in diameter. This layer is

134 suggested to be deposited from a dilute 'surge'-like PDC. On top of it, with a transitional contact,

135 a ~30 m thick, very poorly sorted, massive lapilli tuff was deposited. The average diameter of the

136 pumices is 5 cm. The largest pumices exceed 20 cm in diameter. Lithics are rare and their

137 diameter is up to ~15 cm. The matrix:clast ratio is approximately 80:20. This unit is suggested to

138 be a non-welded ignimbrite. The upper contact of the ignimbrite succession could not be located,

139 because its upper boundary is a recent erosional surface.

140 At Bogács, samples were collected from a slightly welded ignimbrite. The age of this deposit is

141 17.2±2.3 (Márton and Pécskay 1998). Detailed volcanology and petrology of this ignimbrite was

142 given by Czuppon et al. (2012), who subdivided the deposit into two subunits based on color,

143 degree of welding, and pumice characteristics. The Lower Welded Pyroclastic Unit (LWPU) is

144   characterized by a 8-9 m thickness, reddish grey color, ~40 cm maximum pumice diameter at the

145   top, and increasingly welded appearance toward its upper contact. The Upper Mixed Ignimbrite

146   Unit (UMIU) overlies the LWPU with a continuous transition. The UMIU is a 15-17 m thick, red

147   massive lapilli tuff with a chemically bimodal pumice and glass shard populations. It contains

148   pumice lapilli, scoria clasts, and mixed pumices (Czuppon et al 2012). At the site considered in

149   this study the thickness of the ignimbrite is 6.5 m, thus covering the lower part of the LWPU of

150   Czuppon et al. (2012). The upper boundary is an erosional surface, thus the original thickness of

151   the deposit could not be constrained here either. The ignimbrite overlies a fine tuff unit with a

152   sharp contact. From the base to the top of the outcrop a progressive variation in the degree of

153   welding can be traced via the color and the hardness of the deposit. Just above the basal contact,

154   the non-welded, friable lowermost part is 0.2 m in thickness. Above, the deposit becomes

155   increasingly welded and its color changes from greenish grey to pinkish grey and red. The

156   maximum size of the pumice lapilli are 2 cm along the investigated section. Lithics are rare and

157   have a maximum diameter of 1 cm.

158

159

160   **Methods**

161

162   **Sampling strategy**

163   The goal of the study was to examine the impact of sample position within the deposit – which

164   could be translated to relative cooling rate – on the hydroxyl defect concentration of quartz

165   phenocryst fragments. For this, we sampled two different ignimbrite units at the Bükk Foreland

166   Volcanic Area at North Hungary (Fig. 1 b). Four samples from each natural vertical exposures

167   were taken from various vertical positions above the base of the deposits. The sampled heights

168   are indicated in Table 1, and in Fig. 2. Samples from the lowermost part of the ignimbrites were

169   collected in both sites. Other samples were collected from the following heights above the base:

170   at Eger: 0.5 m, 1.2 m, 10 m; at Bogács: 0.5 m, 1.0 m, 6.5 m.

171

172   **Sample preparation**

173   At both sites the separation of the pumice clasts from the matrix was hindered by a resistant

174   cementation. Only in the case of E-1, which was collected from the friable initial Plinian fall

175   deposit at Eger individual crystals were picked. In all other samples quartz phenocryst fragments

176   were collected from the crushed residue of the whole rock. As a result, phenocryst fragments

177   could originate from the matrix or from the juvenile clasts, too. The matrix is supposed to contain

178   quartz crystals from two different sources. The majority of these quartz crystals in the matrix

179   originated from the fragmentation of pumice clasts during pyroclast transportation and represent

180   a cogenetic population. In addition, there could be some phenocryst fragments which are not

181   cogenetic and incorporated during PDC movement from the nearby formations. A steel crushing

182   device was used to get blocks with approximately one centimeter in diameter, followed by further

183   crushing using a ceramic crushing mortar. The residual debris was washed under running water

184   and then dried at room temperature until most of the moisture disappeared. Further sample

185   preparation to produce doubly-polished quartz wafers suitable for IR measurements was done

186   according to the protocol described in Biró et al. (2016).

187

188   **Quartz characterization**

189   The size and shape of the crystals and the features of inclusions from the quartz phenocrysts were

190   studied under a binocular microscope. The concentrations of ^{7}Li, ^{23}Na, ^{27}Al, ^{39}K, ^{49}Ti were

191   measured at the Geological and Geophysical Institute of Hungary by using a New WaveUP 213

8

192   laser ablation system coupled with a quadrupole ICP-MS, Perkin Elmer Elan DRCII and with the

193   same measurement conditions as explained in Biró et al. (2016).

194

195   **Micro-FTIR methodology**

196   To get quantitative data on the hydroxyl defect concentration of quartz phenocryst fragments

197   unpolarized micro-FTIR (Fourier Transform Infrared) measurements were carried out on

198   unoriented quartz fragments. This methodology offers a practical, but still reasonably accurate

199   tool for analyzing a large number of crystals. At least 23 phenocryst fragments from each

200   sampling level were measured (Table 1). The measurements were carried out at the Hungarian

201   Institute for Forensic Sciences by using a Bruker Vertex 70 spectrometer coupled to a Bruker

202   Hyperion 1000 infrared microscope. Measurements were performed using a 100 μm x 100 μm

203   squared aperture. Spectra were recorded with at least 64 scans between 400 and 4000 cm^{-1} with a

204   nominal spectral resolution of 4 cm^{-1}. Before each spectrum acquisition the quartz wafers were

205   checked for visible mineral, melt or fluid inclusions. The spectra were recorded from sites where

206   such inclusions were absent. The spectra were processed with the OPUS software. In some cases

207   the Atmospheric Compensation tool of OPUS were applied to eliminate the unwanted

208   contribution of atmospheric water vapor to the hydroxyl region. Background correction was

209   performed on each spectrum by using a concave rubberband type correction including at least 2

210   iterations and 64 fitting points. A comparison with manual background corrections indicated that

211   the results are usually the same within analytical uncertainty (±5%; i.e. EA22 crystal fragment)

212   and underestimations beyond analytical uncertainty by the concave rubberband correction may

213   only be present for very hydroxyl- poor samples (i.e. UPM11 crystal fragment). Nevertheless, do

214   not influence the main conclusions of the study. The application of uniform concave rubber band

215   corrections for each sample guarantees more accurate relative comparison since the uncertainty

216   emerging from repeated manual background corrections can be omitted. Integration of hydroxyl

217   defect-related absorbances was performed with the Integration tool of OPUS with "B method"

218   which includes the area above a line connecting the intersections of the lower and upper limits of

219   integration. Thickness of doubly-polished quartz wafers were determined by a MITUTUYO

220   micrometer which has a precision of 1 μm. In some cases the thickness was calculated by using

221   the relation between Si-O-related absorbances and effective sample thickness as described by

222   Biró et al. (2016).

223   The theoretical background for quantitative unpolarized IR spectrometry was introduced by

224   Sambridge et al. (2008) and Kovács et al. (2008), which assumes that the hydroxyl defect content

225   is uniform within and among crystals and the analyzed crystals are unoriented. As we will

226   demonstrate below these conditions are not met perfectly for each sample suite and there we

227   should assume higher uncertainty. The absolute hydroxyl defect contents (in ppm H_2O by weight)

228   can be estimated then according to Equation 1:

229

230     $$C_{OH} = \frac{\sum_{i=0}^{n} A_i^{unpol}}{n} \cdot k \cdot 3$$ (1)

231

232   where A_i^{unpol} is an individual unpolarized integrated absorbance normalized to 1 cm thickness

233   within a given sample suite, k is the calibration factor for polarized light (~0.072±0.015[1] for

234   quartz) and 3 is a constant which relates the average unpolarized integrated absorbance to total

235   polarized absorbance (Kovács et al. 2008; Sambridge et al. 2008). Previous studies demonstrated

236   that if a sufficient number of unoriented crystals is considered for a given minerals (quartz, Biró

---

[1] this is calculated from the ε = 94 000±20 000 L/mol·cm^{-2} extinction coefficient of Thomas et al. (2009) assuming
2650 g/L density for quartz according to k=$\frac{c \cdot M_A}{\rho \cdot \varepsilon}$ where c = 10^6, and M_A is the molar weight of water (18.02 g)

237   et al. 2016; olivine, Kovács et al. 2008, Bali et al. 2008) than the total polarized absorbance can

238   be approximated within 10%. For some sample suites where deviations from the ideal

239   distribution of unpolarized absorbance were found this uncertainty in the estimation of the total

240   polarized absorbance can be up to 20%. Consequently, generally if conditions for the application

241   of the unpolarized methodology are ideal the uncertainty in the absolute hydroxyl defect content

242   should be lower, than 25% by using the error propagation formula of Liu et al. (2006), which

243   includes the uncertainty of the individual measurements and the calibration factor as well.

244   In addition, from a set of unpolarized absorbances the principal polarized absorbances can be

245   estimated based on Equations 2 (i.e., Equations 70 in Sambridge et al. 2008):

246

247    $A_a^{pol} = 3A_{unpol}^{avg} - 2A_{unpol}^{max}$

248    $A_b^{pol} = 2(A_{unpol}^{min} + A_{unpol}^{max}) - 3A_{unpol}^{avg}$ (2)

249    $A_c^{pol} = 3A_{unpol}^{avg} - 2A_{unpol}^{min}$

250

251   This permits to assess how well the estimated principal polarized absorbances for each quartz

252   sample suite resembles the theoretical ones. For quartz which is dominated by Al-related

253   hydroxyl defects it is known that there are equal principal polarized absorbances in the indicatrix

254   section perpendicular to the c-axis, whereas there is no or only negligible absorbance parallel to

255   the c-axis (Aines et al. 1984; Stalder and Konzett 2012; Fig. 3 a, b, c, d). From these estimated

256   principal polarized absorbances unpolarized absorbances also can be calculated for any direction

257   of the incident light applying Equation 3 (Fig. 3 e, f, g).

258

259 $A_{unpol}(\phi,\psi) = \frac{1}{2}[A_a^{pol} (\cos^2\phi\cos^2\psi + \sin^2\psi) + A_b^{pol} (\cos^2\phi\sin^2\psi + \cos^2\psi) + A_c^{pol}\sin^2\phi]$

260   (3)

261

262 Using this relation a Monte Carlo simulation can be implemented with the generation of random

263 ψ and ϕ angles (Fig. 3 e) which define spatially uniform points on a sphere. These two angles

264 represent the direction of the incident light with respect to the principal polarized absorbances.

265 Supplementary Material 1 can generate unpolarized absorbances for random directions of the

266 incident light. From these 10 000 calculated unpolarized absorbances a distribution plot can be

267 generated which shows what the ideal theoretical distribution of unpolarized absorbances is. If

268 this ideal distribution is compared to the empirical one it can be assessed how reliably the

269 conditions for the application of the unpolarized methodology are fulfilled. Thus, it may be

270 revealed if there are intra- and intergranular variations of hydroxyl defect concentrations and/or

271 the crystals are not perfectly unoriented. In addition, to get information on the potential

272 intragranular variations of hydroxyl defect concentrations measurements along transects on

273 individual phenocryst fragments were done. During these measurements transects with 4 or 5

274 points were analyzed. Each measurement point was carefully selected to avoid the contribution of

275 visible fluid- and silicate melt inclusions.

276

277

278   **Results**

279

280 **Quartz characterization and trace element concentrations**

281   Basic characteristics of investigated quartz crystals are presented in Table 1. Representative

282   microphotograps from quartz phenocrysts are presented in Fig. 4. At Eger whole, euhedral

283   phenocryst and fragments with abundant cracks are also common. Whole, bipyramidal crystals

284   are rare in E-1 sample which was collected from the initial Plinian fall deposit. The phenocryst

285   fragments are 1.9 mm on average, and the largest fragments are 4 mm in diameter in E-1. In the

286   E-2, E-3 and E-4 samples phenocryst fragments are smaller, in general 1.4 - 1.5 mm in diameter.

287   At Bogács, the quartz crystals are generally smaller than 1 mm. At the base of the ignimbrite, the

288   average crystal size is 1 mm. BG-2, BG-3 and BG-4 samples from higher vertical positions are

289   characterized by 0.6 - 0.8 mm average quartz diameter. At Bogács, fragments are rare, most of

290   the grains are euhedral, bipyramidal crystals. Resorption at crystal margins can only be seen on

291   the largest crystals from the base of the ignimbrite. Smaller crystals do not show such features. At

292   Eger, these resorption features are absent. In the crystals from Eger rounded and hourglass melt

293   inclusions are common especially in E-1 and E-2 samples. Melt and fluid inclusions are rarer in

294   E-3 and E-4 samples. At Bogács, large, irregular melt inclusions are abundant in the quartz

295   crystals from just above the lower contact, in the other levels (BG-2, BG-3, BG-4) inclusions are

296   rare and small. Biotite inclusions are rare at both sites.

297   The concentrations of alkaline elements as ^{7}Li, ^{23}Na, ^{39}K, as well as ^{27}Al and ^{49}Ti along transects

298   and relative standard deviations are presented in Supplementary Material 2. Systematic changes

299   in the concentrations of certain trace elements along transects or between crystals from various

300   height above the base were not observed. In most of the phenocryst fragments, the concentration

301   of the measured elements (N) is generally below 500 N/10^{6}Si, except Li, which is always higher,

302   than 860 Li/10^{6}Si. The relative standard deviations are generally higher than 20% for all elements

303   except H, thus they display detectable inhomogeneities. The highest average trace element

304   concentration was measured in BG-4 phenocryst fragments. The concentration of Al varies

13

305   between 140 and 1624 Al/10^6 Si and shows homogeneity along transects. However, some higher

306   outlier values can be seen in nearly all phenocryst fragments. Ti concentrations vary between 33

307   and 120 Ti/10^6Si. In BG-2 phenocryst fragment the concentration of Ti is as high as 110 Ti/10^6Si

308   in the core, but ~35 Ti/10^6Si at themargins. The concentration of Ti is lower than 55 Ti/10^6Si in

309   the BG-1 and BG-3 phenocryst fragments. In the case of alkalis the average concentrations are

310   proportional to the atomic mass of the particular element. Among alkalis, potassium showed the

311   smallest variation within the phenocryst fragments, the lowest concentration is 90 and the highest

312   is 593 K/10^6Si. The concentration of Na is generally lower than 500 Na/10^6Si, however, in E-1

313   and BG-4 phenocryst fragments there are some higher values too. Lithium shows an average

314   concentration within all phenocryst fragments between 862 and 3938 Li/10^6Si, except BG-4,

315   where its concentration is generally higher.

316

317   **Results of the FTIR measurements**

318   **Main absorbance features.** The average spectra for samples from various heights above the

319   lower contact of the two ignimbrites are presented in Fig. 2. Supplementary Material 3 contains

320   all the spectra for all analyzed phenocryst fragments. In all spectra the most pronounced

321   absorption feature is the triplet centered around 3378 cm^{-1} with two minor bands at 3430 and

322   3315 cm^{-1}. In Eger samples a weak absorption feature at 3483 cm^{-1} could also be observed, which

323   is absent in Bogács samples. A broad and weak absorbance feature at ~3200 cm^{-1} is typical in all

324   samples. In BG-2 this very weak broad band is centered around 3250 cm^{-1}.

325   **Correspondence between theoretical and estimated principal polarized absorbances.** In the

326   methodological section it was demonstrated how principal polarized absorbances can be

327   estimated from the measured unpolarized absorbances according to Equation 2. For this

328   estimation the maximum, minimum and average unpolarized absorbances can be calculated for

14

329   each sample. In Table 2 we estimated the principal polarized absorbances for each sample suite.

330   The calculations yield very similar results. The results indicate that there are two, similar

331   principal polarized absorbances and a third one which is consistently much less than these two

332   and its absolute value is close to zero. These results resemble very closely the ideal principal

333   polarized absorbances of quartz (Fig. 3 b). For a few samples, nevertheless, we experienced

334   significant deviations from the ideal ratio of the principal polarized absorbances. It is particularly

335   true for BG-1 and BG-2 samples, where the estimated values are very far from the ideal ones.

336   Similar discrepancy is present for E-1, however, in this case the deviation is not as significant.

337   For the BG-2 sample we found two extremely low unpolarized absorbances (11.5 and 11.7 cm^{-2})

338   with which omission reasonable agreement is established between empirical and ideal principal

339   absorbance values. Similarly if a very high outlier unpolarized absorbance (57.9 cm^{-2}) is omitted

340   for E-3, the correspondence between empirical and theoretical principal polarized absorbances

341   becomes more encouraging. For these samples the overall analytical uncertainty in the hydroxyl

342   defect concentrations is higher ($\sim 30 - 35\%$).

343   Generally good correspondence was found between the calculated maximum principal polarized

344   absorbances and the maximum unpolarized absorbances as well (Table 2).

345   **Distribution of unpolarized absorbances and its relation to the theoretical ones.** In different

346   indicatrix sections the unpolarized absorbance varies between a minimum and maximum value,

347   when the infrared radiation travels perpendicular and parallel to the c-axis respectively. We used

348   Equation 3 to generate 10 000 unpolarized absorbance values for randomly oriented directions of

349   the incident light by using the Monte Carlo simulation in Supplementary Material 1. During this

350   calculation we assumed that the maximum polarized principal absorbances are equal to the

351   calculated average maximum principal polarized absorbances and the minimum polarized

352   absorbance is zero (Table 2). The calculated theoretical distributions are then plotted

15

353   simultaneously with the empirical distributions for each sample (Supplementary Material 4).

354   Empirical distributions were computed from the measurements on individual phenocryst

355   fragments (Supplementary Material 5). Generally very good correspondence is found between the

356   histograms of measured and theoretical unpolarized absorbances for the E-4, BG-4, BG-3

357   samples. The correspondence is also reasonable for E-1 and E-2 samples. The other quartz suites

358   show smaller or higher deviation from the expected theoretical distribution. If we do not consider

359   the higher outliers in E-3 and the lower outlier values in BG-2 the difference between obtained

360   and theoretical distributions are not very profound. The most significant deviation in the

361   distribution of measured unpolarized absorbances from the theoretical predictions is present in

362   the lowermost BG-1 sample at Bogács, which was collected from just above the base of the

363   ignimbrite.

364   **Hydroxyl defect concentrations along transects.** To check the intragranular variability of

365   hydroxyl defect concentration we performed measurements along transects (Supplementary

366   material 2 and 6). In general, the intragranular heterogeneity of the hydroxyl defect concentration

367   is negligible. The relative standard deviations of hydroxyl defect concentrations are lower than

368   10%. However, there are some phenocryst fragments, where the relative standard deviation is

369   between 10 and 20%. The highest relative standard deviations can be observed for the E-4

370   sample.

371   **Hydroxyl defect concentrations as a function of height above the base.** Hydroxyl defect

372   concentrations show a clear decreasing trend from the base of the deposits upwards (Fig. 2, Fig.

373   5, Table 1). Results of measurements on individual phenocryst fragments are presented in

374   Supplementary Material 5. At both sites the highest hydroxyl defect concentrations are observed

375   in quartz phenocryst fragments from just above the lower contacts. The hydroxyl defect

376   concentration at the base are 12.1 ppm at Eger and 12.8 ppm at Bogács. The lowest hydroxyl

16

377   defect concentrations were observed in the samples from the highest stratigraphic position above

378   the base. The lowering of the hydroxyl defect concentrations with height above the base is

379   different at the two sites. In the case of Eger this decreasing trend is more smooth and gradual

380   (Fig. 5).

381

382

383   **Discussion**

384   **Interpretation of the infrared spectra**

385   The average spectra from various heights above the lower contact of the two ignimbrites are

386   presented in Fig. 2. Supplementary Material 3 contains the spectra for all analyzed phenocryst

387   fragments. In all spectra the most pronounced absorption feature is the triplet centered around

388   3378 cm^{-1} with minor bands at 3430 and 3315 cm^{-1} which are related to the substitution of $H^+ +$

389   Al^{3+} for Si^{4+} (Kats 1962; Thomas et al. 2009; Müller and Koch-Müller 2009). In Eger samples the

390   weak absorption feature at 3483 cm^{-1} is caused by coupled Li-related hydroxyl defects (Aines and

391   Rossmann 1984; Baron et al. 2015, Frigo et al 2016). This absorbance feature is absent in Bogács

392   samples. The broad and weak absorbance feature at ~3200 cm^{-1} is typical in all samples. This

393   band is possibly related to the absorption of water or hydroxyl on sample surface (Biró et al.

394   2016). In the case of BG-2 a weak broad band centered around 3250 cm^{-1} is present. The sharp

395   individual bands are situated on this broad feature, which is known to be related to bonding

396   between hydrogens of molecular water and silica framework (e.g., Biró et al. 2016).

397

398   **Inter- and intragranular heterogeneity of hydroxyl defect concentrations**

399   **Statistical evaluation of unpolarized absorbances.** We considered the i) correspondence

400   between theoretical and estimated principal polarized absorbances; ii) correspondence between

17

401   the distribution of measured unpolarized absorbances and the theoretical one from 10 000 random

402   incidence directions. The calculated principal absorbances, besides the basal samples (E-1, E-2,

403   BG-1, BG-2), are close to the theoretically expected relative values (Table 2). It implies, that

404   generally the inter- or intragranular variations of hydroxyl defect concentrations as well as the

405   deviation from the ideal unorientation of quartz crystals are negligible.

406   Another way to assess whether intra- and intergranular heterogeneities in hydroxyl defect

407   concentration are present and if quartz crystals are indeed unoriented is to look at the histograms

408   showing the distribution of measured and theoretical unpolarized absorbances (Supplementary

409   Material 4). Although, we could expect differences due to the relatively small unpolarized

410   absorbance populations (~ 30) compared to the theoretical one (10 000) and the partial

411   polarization of the unpolarized light the resemblance for the majority of the sample suites is

412   encouraging. This implies, similar to the previous methodology, where principal absorbances are

413   estimated from the unpolarized measurements that generally the quartz crystal are indeed

414   unoriented and inter- and intragranular inhomogenity of hydroxyl defect concentration is not

415   significant. However, the distribution of unpolarized absorbances for the basal samples (E-1; BG-

416   1) is further from the theoretically expected one which is most striking for BG-1.

417   The statistical evaluation of unpolarized IR results imply, that the unpolarized methodology is

418   able to quantify accurately the hydroxyl defect concentration of quartz phenocryst fragments

419   within ignimbrites. The presence of intergranular heterogenities of hydroxyl defect

420   concentrations at the basal part of ignimbrites and the lack of such features in the uppermost

421   samples (E-4, BG-4) imply the complex processes which play role in affecting the hydroxyl

422   defect concentration of crystals in PDC deposits.

423   **Concentration of hydrogen and trace elements along transects.** Intragranular variabilities of

424   hydroxyl defect concentration via measurements along transects are presented on Fig. 6 and on

425 Supplementary material 2 and 6. In general, the intragranular heterogeneity of the hydroxyl

426 defect concentration is negligible and only slightly exceeds 10% (but never 20%) in a few grains,

427 which is only marginally above analytical uncertainty. There are slight inhomogeneities in

428 samples E-2, E-3, E-4 and BG-2, where the relative standard deviation of hydroxyl defect

429 concentration along transects slightly exceeds 10%. In the case of sample E-4, which was

430 collected from the internal part of Eger ignimbrite the hydroxyl defect concentration is 3.3 ppm.

431 Thus, here the higher relative standard deviations of hydroxyl defect concentration may be

432 related to the challenge of analyzing accurately the concentration of hydroxyl defects at such low

433 concentration level. For samples E-2, E-3 and BG-2 the slightly higher standard deviations in

434 hydroxyl defect concentration may be the result of real inhomogenities, because the hydroxyl

435 defect concentrations are higher (> 6.1 ppm) and as such less affected by the analytical error.

436 Note that these are also the samples for which the distribution of unpolarized absorbances

437 revealed more considerable deviations from the ideal one, confirming the existence of possible

438 heterogeneities in hydroxyl defect concentrations.

439 The substitution of Al^{3+} for Si^{4+} ideally requires an additional monovalent cation for charge

440 compensation, such as K^+, Na^+, Li^+ or H^+ (e.g., Müller and Koch-Müller 2009). Based on

441 Supplementary Material 2 there is no correlation between the concentrations of Al, K, Na, Li and

442 hydroxyl defects. As we demonstrated above the concentration of hydroxyl defects is almost

443 homogeneous and independent from other trace elements along transects. The relative standard

444 deviation of hydroxyl defect concentration is generally lower, than 10%. On the contrary, other

445 trace elements show pronounced heterogeneities and relative standard deviations higher, than

446 20%. Present results confirm the observations of Biró et al. (2016), that in ignimbrite-hosted

447 quartz phenocryst fragments the concentration of hydroxyl defect is low, homogeneous and do

448 not depend on the concentration of other trace elements. These results imply that Al impurities

19

449   are generally compensated with monovalent alkalis, and only a minute amount of H could be

450   incorporated in combination with Al. The concentration of H is always lower, than 90 $H/10^6Si$,

451   while the bulk concentration of monovalent alkalis and lithium is between 1190 and 5610

452    $N/10^6Si$, thus higher with two orders of magnitude.

453

454   **Decreasing amount of hydroxyl defect concentrations with height above the base of**

455   **ignimbrites**

456   **Implications on post-depositional diffusional loss of hydrogen from quartz phenocryst**

457   **fragments.** At both sites hydroxyl defect concentrations show decreasing trend as a function of

458   height above the base (Fig. 2, 5). The lowering is more smooth at the non-welded Eger ignimbrite

459   and more abrupt at Bogács. These features implies that phenocryst fragments could lost their

460   initial hydroxyl defect concentration via diffusion after deposition at initially high typical

461   ignimbrite temperatures (>500°C; Kent et al. 1981; McClelland and Druitt 1989; McClelland et

462   al. 2004; Bardot 2000, Zanella et al. 2008). The highest hydroxyl defect concentrations, which

463   are slightly higher, than 12 ppm can be seen at the base of the deposits, where the cooling was

464   fast enough to prohibit significant hydrogen diffusion via the cooling effect of the underlying

465   colder deposits. Relatively fast cooling may take also place in the uppermost part of the PDC

466   deposit too due to contact with the atmosphere. This effect however could not be observed in the

467   investigated ignimbrites, because uppermost layers were eroded and recent upper boundaries are

468   erosional surfaces. Depositional temperature of ignimbrites can reach 850°C (e.g., Banks and

469   Hoblitt 1981, 1996). High temperature emplacement of PDC deposits could be determined via

470   identifying welding-related textural changes in the internal part of thick ignimbrites, which are

471   the result of structural collapse of vesiculated pumices because of high temperature and mass

472   load (McPhie et al. 1993). For example, welding is possible in the central part of thick

20

473   ignimbrites (at 30 - 40 bar pressure) at 500 - 650°C temperatures, if glass shards and pumices

474   have calc-alkaline major element composition (Yagi 1966). If high emplacement temperature-

475   related textural changes are not visible emplacement temperature could be determined by using

476   Natural Remanent Magnetization (NMR) measurements. Using NRM techniques many studies

477   revealed that the temperature within thick non-welded ignimbrites ranges between 150 - 500°C

478   (Kent et al. 1981; McClelland and Druitt 1989; McClelland et al. 2004; Bardot 2000, Zanella et

479   al. 2008). Numerical modeling – based on typical ignimbrite temperatures, specific heat transport

480   and thickness – also has shown, that high temperature (> 300°C) can be maintained for several

481   hundred days in the internal part of thick ignimbrites (Riehle 1973; Riehle et al. 1995; Wallace et

482   al. 2003). The cooling rate of ignimbrites varies from 10^{-1}°C s^{-1} at the base to 10^{-6} to 10^{-8}°C s^{-1}

483   (or 0.3°C $year^{-1}$) in the interior of several tens of meters thick PDC deposits (Wallace et al. 2003).

484   Above 400°C and presumably at much lower hydrogen activity the 'original' hydroxyl defects

485   can diffuse out from the phenocryst fragments (Kronenberg et al. 1986). The diffusion speed of

486   Al-OH hydroxyl defects in quartz as a function of temperature shows an Arrhenius relation (Kats

487   1962; Kronenberg et al. 1986; Kronenberg and Kirby 1987). At 400 - 500°C, which is believed as

488   a typical depositional temperature for non-welded ignimbrites the diffusivities of protons in

489   quartz are 5 x 10^{-15} and 2.4 x 10^{-14} m^2/s respectively (Kats 1962). The two ignimbrites are

490   characterized by different physical volcanological properties as shown by different degree of

491   welding, which imply different depositional temperatures. The contrasting degree of welding is

492   coupled with contrasting amounts of hydroxyl defect deficit as a function of height above the

493   base (Fig. 5).

494   **Modelling diffusional loss of hydrogen from quartz crystals during ignimbrite cooling.** To

495   test the effectiveness of diffusion induced dehydration after emplacement at typical ignimbrite

496   temperatures a model describing the lowering of initial hydroxyl defect concentration (C_0) of

497   quartz crystals has been constructed (Supplementary Material 7). This model calculates the ratio

498   of the initial hydroxyl defect concentration at the time of hot deposition and the hydroxyl defect

499   concentration during cooling (C_i/C_0) at certain levels in the ignimbrite. Temperature (T) is the

500   main factor affecting the diffusion coefficient (D) of hydrogen in quartz at constant pressure and

501   hydrogen fugacity (Kats 1962, Kronenberg et al. 1986). Thus, first, the average temperature

502   $T(z,t)$ for discrete, 200 s time intervals for certain heights above the base within the ignimbrite

503   were computed by using Equation 9 of Wallace et al. (2003):

504

505   $$T(z,t) = T_{atm} + \frac{T_p - T_{atm}}{2} \cdot \left[erf \frac{z_1 - z}{\sqrt{4Kt}} + 2erf \frac{z}{\sqrt{4Kt}} - erf \frac{z_1}{\sqrt{4Kt}} \right] + \frac{T_g - T_{atm}}{2} \cdot \left[erf \frac{z_1 + z}{\sqrt{4Kt}} - erf \frac{z_1 - z}{\sqrt{4Kt}} \right].$$

506   (4)

507

508   ,where $T(z,t)$ is the temperature at a given height above the base at a given time (t), T_p, T_{atm} and

509   T_g is the temperature of the PDC deposit, the ambient atmosphere and the underlying ground, z_1

510   is the thickness of the PDC deposit, z is the difference between the height of the particular level

511   above the ground and the height of the upper boundary of the PDC deposit above the ground, K is

512   a thermal diffusivity constant and t is the elapsed time since emplacement. Post depositional

513   thermal history of the sampled heights above the base (Eger: z_1-z=0.05, 0.5, 1.2, 10.0 m; Bogács:

514   z_1-z=0.05, 0.5, 1.0, 6.5 m) were determined. Several model runs had constructed with different

515   thickness (z_1) and initial temperatures (T_0), which were selected by considering the actual –

516   erosion-related – deposit thicknesses as minimum original thicknesses and typical ignimbrite

517   emplacement temperatures (Kent et al. 1981; McClelland and Druitt 1989; McClelland et al.

518   2004; Bardot 2000, Zanella et al. 2008). $T(z,t)$ were determined for Eger ignimbrite for z_1=30, 40,

519   50 m and T_0=300, 400, 500, 600°C and for the Bogács ignimbrite for z_1=20, 30, 40 m and T_0=

22

520   400, 500, 600, 700°C. The same heat conductivity constant (K=0.003) for the ignimbrites as in

521   Wallace et al. (2003) was used. After that, D (m^2/s) for each 200 s time interval were determined

522   by extrapolating the D values of Kats (1962) and Kronenberg et al. (1986). Equation 2 in Ingrin

523   et al. (1995) was used to calculate the loss of hydroxyl defect concentration relative to the

524   concentration of the previous bin (C_n/C_{n-1}). During the calculation for simplicity we assumed that

525   the D values can be taken as constant in the 200 seconds long bins:

526    $$\frac{C_n}{C_{n-1}} = \frac{8}{\pi^2}\left[exp\left(-\frac{\pi^2 t}{4L^2}\right)D + \frac{1}{9}exp\left(-\frac{9\pi^2 t}{4L^2}\right)D + \frac{1}{25}exp\left(-\frac{25\pi^2 t}{4L^2}\right)D + \cdots + \frac{1}{917}exp\left(-\frac{917\pi^2 t}{4L^2}\right)D\right]$$

527   (5)

528   According to Equation 5 the C_n/C_{n-1} ratio is affected by D (m^2/s), t (s) and 2L (m), which is the

529   average crystal diameter in meters. Average crystal diameters were determined for each analyzed

530   grain with an optical microscope (Table 1). In the model runs a uniform C_0 was suggested in the

531   entire deposit at the time of deposition which was taken as the highest hydroxyl defect

532   concentrations just above the lower contacts as 12.1 at Eger and 12.8 ppm at Bogács were used as

533   C_0. All model runs were 8 day long, which is enough time for the cooling of the entire deposit

534   below 100°C. Under 100°C D become $<1.2 \times 10^{-17}$, consequently the further dehydration is

535   negligible.

536   The final C_i/C_0 ratio was calculated by simply multiplying the C_n/C_{n-1} values for all respective

537   200 s bins:

538    $$\frac{C_i}{C_0} = \frac{C_2}{C_1} \times \frac{C_3}{C_2} \times \ldots \times \frac{C_n}{C_{n-1}} \qquad (6)$$

539   Thus, the lowering of the initial hydroxyl defect concentration for the investigated heights above

540   the base could be determined for each combination of T_0 and z_1. The calculation and the results

541   of all runs are presented in Supplementary Material 7.

542   Measured and modelled hydroxyl defect concentrations for investigated heights above the base of

543   Eger and Bogács ignimbrites are presented in Fig. 5. The results of modelling show, that at

544   typical emplacement conditions for ignimbrites if T_0 is 500°C and z_1 is 40 m C_i could be ~60 -

545   50% of C_0 at 10.0 (Eger) and 6.5 m (Bogács) respectively. This implies, that post-depositional

546   dehydration could describe the upward decreasing trend of hydroxyl defect concentrations within

547   ignimbrites. However, all modelled relative concentration differences between E-2 and E-3 and

548   BG-2 and BG-3 are significantly lower than 10%, while measured ratios are significantly higher:

549   ~50 and 70% respectively. The modelled dehydration could not account for the low values a (~3

550   ppm) at the uppermost levels. These differences between measured and modelled values imply,

551   that contrasting post-depositional thermal histories and different average crystal diameters only

552   could not cause such difference in hydroxyl defect concentration between 0.5 and 1.0 and 1.2 m

553   levels above the base. Besides the contrasting depositional temperature, which is evident from

554   ignimbrite textures possibly the lower average diameter of crystals at Bogács, than at Eger (Table

555   1) also contribute to the more abrupt decrease of structural hydroxyl concentration at Bogács.

556   The clear inverse relation between the concentration of hydroxyl defect content of quartz crystals

557   and height above the base could imply the dominant but not exclusive role of post-depositional

558   dehydration.

559   **The possible role of pre-eruptive and pre-depositional history and phenocryst**

560   **characteristics on final hydroxyl defect concentration.** Several additional factors could

561   contribute to the observed difference between measured and modelled hydroxyl defect

562   concentrations at a particular height above the base in pyroclastic successions. Both the initial

563   concentration of structural hydroxyl (i.e. that in the magma chamber) and effective diffusional

564   loss of hydrogen could be different at various heights above the base of the deposit. This is

565   because of initial zonation in the magma chamber, contrasting pre-depositional thermal history

566   and fracture and melt or fluid inclusion density in quartz crystals.

567   The concentration of hydroxyl defects in quartz crystals in magma chambers is controlled

568   principally by pressure, temperature and hydrogen activity (Stalder and Konzett 2012). Because

569   large silicic magma chambers show zonation in pressure, temperature (Hildreth 1979) and

570   hydrogen activity (Anderson et al. 1989, Dunbar et al. 1992, Wallace et al. 1999) differences in

571   hydroxyl defect concentration of quartz crystals prior to eruption are likely to occur. The

572   temperature and pressure decrease while the hydrogen activity is usually increases towards the

573   upper and peripheral parts of the magma chamber. This results in higher structural hydroxyl

574   defect content of (quartz) phenocryst in the upper and peripheral parts of the magma chamber. In

575   addition it is also very likely that melt inclusions are more frequently entrapped in these

576   presumably more rapidly and readily crystallizing zones. This is in accordance with the

577   experimental findings that the Al-related hydroxyl defect concentration negatively correlate with

578   pressure and temperature (Stalder and Konzett 2012, Baron et al. 2015), resulting in higher

579   concentration of hydroxyl in the relatively cold uppermost part of silicic magma chambers. The

580   observed difference in distribution, shape and composition of quartz-hosted melt inclusions also

581   reflect similar tendencies in hydrogen activity according to the position in the magma chamber

582   (Anderson et al. 2000, Peppard et al. 2001). Melt inclusions from the Bishop Tuff show

583   decreasing total H_2O content (which includes both molecular H_2O and OH^-) from ~6 wt. % at the

584   upper part to ~4 wt. % at the lower part of the magma chamber (Skirius et al. 1990).

585   Thus, in a huge silicic magmatic system with significant vertical extensions quartz phenocrysts

586   from different depths of the magma chamber possibly take up contrasting amount of hydrogen.

587   After eruption the deposition of explosive volcanics may reverse this original zonation of

588   hydroxyl defect and water content in the magma chamber. This is because the upper parts of the

589   magma chamber will be erupted and then re-deposited first followed by the deeper parts.

590   Consequently quartz crystals at the lowermost part of the succession will contain the highest

591   amount of hydroxyl defects.

592   In addition to the pre-eruptional zonation in the magma chamber structural hydroxyl defect

593   concentrations in quartz crystals can be modified also during eruption and pyroclastic

594   transportation prior to PDC deposition. The Arrhenius relation between temperature and D (m^2/s)

595   of Al-OH hydroxyl defects in quartz (Kats 1962; Kronenberg et al. 1986; Kronenberg and Kirby

596   1987) highlight the potential of effective dehydration upon initial >600°C temperature during and

597   just after the eruption. Eruption temperatures in Plinian eruptions related to silicic caldera

598   systems can be as high as 700-850°C according to Ti-in-quartz thermometry (e.g. Wark et al.

599   2007; Shane et al. 2008; Matthews et al. 2012). At such high temperatures hydrogen diffusion in

600   quartz is 3 x 10^{-12} and 2 x 10^{-11} m^2/s respectively (Kronenberg et al 1986). Thus, it is obvious that

601   limited diffusional loss of hydrogen may also occur during the eruption and before final

602   deposition. Hovewer, the ratio of hydroxyl defect concentration before the eruption and at the

603   time of emplacement is possibly different for particular heights above the base of the pyroclastic

604   succession. The hydroxyl defect content, which is the closest to the concentration was

605   equilibrated in the magma chamber could be measured at the base of PDC deposits or in fall

606   deposits, where the cooling rate can be as fast as 1–10°C s^{-1} during pyroclast transportation

607   (Wallace et al. 2003). It is likely that the original hydroxyl defect content of phenocrysts with

608   slower cooling rate may only be constrained by rehydration experiments as presented by Weis et

609   al. (2015) and Weis et al. (2016) in the case of volcanic pyroxenes.

610   Contrasting pre-depositional thermal histories of quartz crystals are suggested to be more

611   important at Eger, where E-1 was collected from the initial Plinian fall layer, E-2 from just above

612   the initial cross-bedded PDC deposit and E-3 and E-4 from the main massive lapilli tuff mass of

26

613 the ignimbrite. The three distinct parts of the ignimbrite succession are possibly characterized by

614 particular pre-depositional thermal histories. The initial 700 - 800°C temperature of Plinian

615 eruption columns able to cooling rapidly with $1 - 10$°C s^{-1} cooling rate upon pyroclast

616 transportation in ambient air (Wallace et al. 2003). The cooling was also relatively fast during the

617 flowage of the initial dilute, 'surge-like' phase of the PDC event, where the turbulent PDC mixed

618 with the ambient air (Branney and Kokelaar 1992). On the contrary, during large-scale PDC-

619 forming explosive eruptions quartz crystals are supposed to be transported in a ground-hugging,

620 much more dense regime, which do not mix significantly with ambient air, thus loose only the

621 fraction of the initial heat (Branney and Kokelaar 1992). During the 1980 eruption of Mt. St.

622 Hellens temperature within the PDC dropped immediately to ~700°C from the magmatic 950°C

623 within few hundreds of meters, but remained constant at 700°C during further flowage (Banks

624 and Hoblitt 1981). It is possible, that original hydroxyl defect concentration (C_0) was different for

625 different parts of the Eger deposit because of the contrasting thermal histories prior to deposition.

626 A higher C_0 for the Plinian fall layer (E-1) and for the initial dilute, surge-like part (E-2) and a

627 lower one for the main mass of the PDC (E-3 and E-4) is conceivable. These differences in C_0

628 could cause the observed abrupt change between the hydroxyl defect content of E-2 and E-3.

629 The modification of original magmatic hydroxyl defect content of quartz crystals during and after

630 PDC emplacement is a complex issue, in which hydrogen-leakage from fluid and melt inclusions,

631 shortening of effective diffusion paths according to crystal size or by the presence of microcracks

632 could all have their influence on the variation of structural hydroxyl content. Melt and fluid

633 inclusions are typical in both investigated ignimbrites, especially at the two lowermost levels just

634 above the base (E-1, E-2, BG-1, BG-2). The fact that melt inclusions are more abundant at the

635 base may reflect the original magma chamber zonation where the entrapment of inclusions was

636 more probable at the upper part of the chamber where crystallization was more intense due to the

637 higher temperature gradient and lower pressures. Hydrogen can leak from fluid and melt

638 inclusions into the quartz host, especially when dislocations, imperfections or microcracks are

639 present in the crystals (Bakker and Jansen 1990, 1994; Heggie 1992; Mavrogenes and Bodnar

640 1994; Severs et al. 2007, Bakker 2009). At the base of the PDC deposits (E-1, E-2, BG-1, BG-2)

641 besides the incorporation of xenocrystals with contrasting hydroxyl defect content, hydrogen

642 leakage from abundant melt and fluid inclusions may also account for the observed

643 heterogeneities in structural hydroxyl content (Supplementary Material 4). The presence of slight

644 inhomogeneities of hydroxyl defect concentration especially in BG-2, BG-3 crystals along

645 transects also confirm the possibility of hydrogen leakage from melt and fluid inclusions. Results

646 of diffusion modelling (Fig. 5) demonstrate, that the pronounced difference of the hydroxyl

647 defect content of quartz crystals between E-2 and E-3 and BG-2 and BG-3 samples could not be

648 the result only of contrasting cooling histories and average grain sizes. This difference may also

649 be the result of the gain of hydrogen from melt and fluid inclusions in E-2 and BG-2 quartz

650 crystals.

651

652

653 **Implications**

654 This study demonstrates that hydroxyl defect content of quartz phenocryst fragments within two

655 Miocene ignimbrites show decreasing trend with height above the base from ~12 to ~3 ppm. The

656 rate of concentration lowering with height above the base is contrasting at the two deposits. The

657 slightly welded ignimbrite, which believed to deposited at higher temperature show more abrupt

658 lowering of hydroxyl defect concentration with height above the base. This imply, that the

659 lowering of hydroxyl defect content of quartz crystals towards the middle of thick ignimbrites is

660 mainly driven by post-depositional dehydration via diffusional loss.

661 Several model runs on dehydration were performed by considering typical ignimbrite

662 temperatures (T_0=300-700°C) and thicknesses (z_1=30-50 m) to investigate the amount of

663 hydrogen loss during cooling at the investigated heights above the base of the ignimbrites. The

664 results demonstrate, that only the contrasting cooling rate and average crystal diameters of

665 different vertical levels within the ignimbrites could not describe their relative hydroxyl defect

666 contents. This imply, that besides the principal role of post-depositional dehydration other

667 factors, such as magma chamber zonation, syn-eruptive and pre-depositional thermal history and

668 inclusion and microcrack density of phenocrysts could all play an important role in affecting the

669 final amount of hydroxyl defects in quartz.

670

671

672 **Acknowledgment**

679

680

681 **References**

682 Aines, R.D., and Rossman, G.R. (1984) Water in minerals? A peak in the infrared. Journal of

683 Geophysical Research: Solid Earth, 89, 4059–4071.

684 doi: 10.1029/JB089iB06p04059

29

685

686   Aines, R.D., Kirby S.H., and Rossman G.R. (1984) Hydrogen speciation in synthetic quartz.

687   Physics and Chemistry of Minerals, 11, 204–212.

688

689   Anderson, A.T. Jr., Newman, S., Williams, S.N., Druitt, T.H., Skirius, C., and Stolper, E. (1989)

690   H_2O, CO_2, Cl, and gas in Plinian and ash-flow bishop rhyolite. Geology, 17, 221–225.

691

692   Anderson, A.T. Jr., Davis, A.M., and Lu, F. (2000) Evolution of Bishop Tuff rhyolitic magma

693   based on melt and magnetite inclusions, and zoned phenocrysts. Journal of Petrology, 41, 449–

694   473.

695

696   Baron, M.A., Stalder, R., Konzett, J., and Hauzenberger, C.A. (2015) OH-point defects in quartz

697   in B- and Li-bearing systems and their application to pegmatites. Physics and Chemistry of

698   Minerals, 42, 53-62.

699   doi: 10.1007/s00269-014-0699-4

700

701   Bali, E., Bolfan-Casanova, N., and Koga, K.T. (2008) Pressure and temperature dependence of H

702   solubility in forsterite: an implication to water activity in the Earth interior. Earth and Planetary

703   Science Letters, 268, 354–363.

704

705   Banks N.G., and Hoblitt R.P. (1981) Summary of temperature studies on 1980 deposits. In P.W.

706   Lipman, and D.R. Mullineaux Ed., The 1980 eruptions of Mount St. Helens. p 295‑314. USGS

707   Prof Paper 1250. USGS,Washington, DC

708

709   Banks, N.G., and Hoblitt, R.P. (1996) Direct temperature measurements of deposits, Mount St.

710   Helens, Washington, 1980–1981. U.S. Geological Survey Professional Paper 1387, 76 p.

711

712   Biró, T., Kovács, I.J., Király, E., Falus, Gy., Karátson, D., Bendő, Zs., Fancsik, T., and Sándorné,

713   K.J. (2016) Concentration of hydroxyl defects in quartz from various rhyolitic ignimbrite

714   horizons: results from unpolarized micro-FTIR analyses on unoriented phenocryst fragments.

715   European Journal of Mineralogy, 29, 313-327.

716   doi: http://dx.doi.org/10.1127/ejm/2016/0028-2515

717

718   Bakker R.J., and Jansen, J.B.H. (1990) Preferential water leakage from fluid inclusions by means

719   of mobile dislocations. Nature, 345, 58-60.

720

721   Bakker R.J., and Jansen, J.B.H. (1994) A mechanism for preferential H_2O leakage from fluid

722   inclusions in quartz, based on TEM observations. Contributions to Mineralogy and Petrology,

723   116, 7-20.

724

725   Bakker, R.J. (2009) Reequilibration of fluid inclusions: bulk diffusion. Lithos, 112, 277–288.

726

727   Bardot, L. (2000) Emplacement temperature determinations of proximal pyroclastic deposits on

728   Santorini, Greece, and their implications. Bulletin of Volcanology, 61, 450–467.

729

730   Branney, M.J., and Kokelaar, B.P. (2002) Pyroclastic density currents and the sedimentation of

731   ignimbrites. Geological Society of London, Memoirs, 27, 143 p.

732

733   Campbell, M.E., Hanson, J.B., Minarik, W.G., and Stix, J. (2009) Thermal History of the

734   Bandelier Magmatic System: Evidence for Magmatic Injection and Recharge at 1.61 Ma as

735   Revealed by Cathodoluminescence and Titanium Geothermometry. Journal of Geology, 117,

736   469–485.

737

738   Capaccioni, B., Corodannosi, N., Harangi, R., Harangi, Sz., Karátson, D., Sarocchi, D., and

739   Valentini, L. (1995) Early Miocene pyroclastic rocks of the Bükkalja Ignimbrite Field (North

740   Hungary) - A preliminary stratigraphic report. Acta Vulcanologica, 7, 119–124.

741

742   Charlier, B.L.A., Morgan, D.J., Wilson, C.J.N., Wooden, J.L., Allan, A.S.R., and Baker J.A.

743   (2012) Lithium concentration gradients in feldspar and quartz record the final minutes of magma

744   ascent in an explosive supereruption. Earth and Planetary Science Letters, 319–320, 218–227.

745

746   Czuppon, Gy., Lukács, R., Harangi, Sz., Mason, P.R.D., and Ntaflos, T. (2012) Mixing of crystal

747   mushes and melts in the genesis of the Bogács Ignimbrite suite, northern Hungary: An integrated

748   geochemical investigation of mineral phases and glasses. Lithos, 148, 71–85.

749

750   Dunbar, N.W., and Hervig, R.L. (1992) Petrogenesis and volatile stratigraphy of the Bishop

751   Tuff-Evidence from melt inclusion analysis. Journal of Geophysical Research: Solid Earth, 97,

752   15129–15150.

753

754   Frigo, C., Stalder, R., and Hauzenberger, C.A. (2016) OH defects in quartz in granitic systems

755   doped with spodumene, tourmaline and/or apatite: experimental investigations at 5–20 kbar.

756   Physics and Chemistry of Minerals, 43, 717-729.

757

758   Götze, J., Plötze, M., and Habermann, D. (2001) Origin, spectral characteristics and practical

759   applications of the cathodo-luminescence (CL) of quartz – a review. Mineralogy and Petrology,

760   71, 225–250.

761

762   Götze, J., Plötze, M., Graupner, T., Hallbauer, D.K., and Bray, C.J. (2004) Trace element

763   incorporation into quartz: a combined study by ICP-MS, electron spin resonance,

764   cathodoluminescence, capillary ion analysis, and gas chromatography. Geochimica et

765   Cosmochimica Acta, 68, 3741–3759.

766

767   Harangi, Sz., and Lukács, R. (2009) On the age of the Harsány ignimbrite, Bükkalja volcanic

768   field, Northern Hungary – a discussion. Central European Geology, 52, 43–50.

769

770   Harangi, Sz., Mason, P.R.D., and Lukács, R. (2005) Correlation of silicic pyroclastic rocks in the

771   Northern Pannonian Basin, Eastern-Central Europe: a geochemical approach. Journal of

772   Volcanology and Geothermal Research, 143, 237–257.

773

774   Hartley, M.E., Morgan, D.J., Maclennan, J., Edmonds, M., and Thordarson, T. (2016) Tracking

775   timescales of short-term precursors to large basaltic fissure eruptions through Fe–Mg diffusion in

776   olivine. Earth and Planetary Science Letters, 439, 58–70.

777

778   Heggie, M. (1992) A molecular water pump in quartz dislocations. Nature, 355, 337–339.

779

780   Hildreth, W. (1979) The Bishop Tuff; Evidence for the origin of compositional zonation in silicic

781   magma chambers. In C.E. Chapin and W.E. Elston, Eds., Ash-flow tuffs: Geological Society of

782   America Special Paper 180, p. 43–75.

783

784   Huang, R., and Audétat, A. (2012) The titanium-in-quartz (TitaniQ) thermobarometer: A critical

785   examination and re-calibration. Geochimica et Cosmochimica Acta, 84, 75–89.

786   doi:10.1016/j.gca.2012.01.009

787

788   Ingrin, J., Hercule, S., and Charton, T. (1995) Diffusion of hydrogen in diopside: Results of

789   dehydrogenation experiments. Journal of Geophysical Research, 100, 15489-15499.

790

791   Kats, A. (1962) Hydrogen in alpha-quartz. Phillips Research Reports, 17, 33–279.

792

793   Kent, D.V., Ninkovitch, D., Pescatore, T., and Sparks, R.S.J. (1981) Paleomagnetic determination

794   of emplacement temperature of the Vesuvius AD 79 pyroclastic deposits. Nature, 290, 393–396.

795

796   Kilgour, G.N., Saunders, K.E., Blundy, J.D., Cashman, K.V., Scott, B.J., and Miller, C.A. (2014)

797   Timescales of magmatic processes at Ruapehu volcano from diffusion chronometry and their

798   comparison to monitoring data. Journal of Volcanology and Geothermal Research, 288, 62–75.

799

800   Kovács, I., Csontos, L., Szabó Cs., Falus, Gy., Bali, E., Benedek, K., and Zajacz, Z. (2007)

801   Paleogene-Early Miocene volcanic rocks and geodynamics of the Alpine-Carpathian Pannonian-

802   Dinaric region: an integrated approach, in Beccaluva, L., Bianchini, G., and Wilson, M., eds.,

803   Cenozoic Volcanism in the Mediterranean Area. Geological Society of America Special Paper,

804   418, 93-112.

805

806   Kovács, I., Hermann, J., O'Neill, H.St.C., FitzGerald, J., Sambridge, M., and Horváth, G. (2008)

807   Quantitative IR spectroscopy with unpolarized light Part II: Empirical evidence and practical

808   application. American Mineralogist, 93, 765–778.

809

810   Kronenberg, A.K., and Kirby, S.H. (1987) Ionic conductivity of quartz: DC time dependence and

811   transition in charge carriers. American Mineralogist, 72, 739–747.

812

813   Kronenberg, A.K., Kirby, S.H., Aines, R.D., and Rossman, G.R. (1986) Solubility and diffusional

814   uptake of hydrogen in quartz at high water pressures: Implications for hydrolytic weakening.

815   Journal of Geophysical Research: Solid Earth, 91, 12723-12744.

816

817   Lesti, C., Porreca, M., Giordano, G., Mattei, M., Cas, R.A.F., Wright, H.M.N., Folkes, C.B., and

818   Viramonte, J. (2011): High-temperature emplacement of the Cerro Galán and Toconquis Group

819   ignimbrites (Puna plateau, NW Argentina) determined by TRM analyses. Bulletin of

820   Volcanology, 73, 1535–1565.

821

822   Liu, X., O'Neill, H.S.C., and Berry, A.J. (2006) The effects of small amounts of H_2O, CO_2 and

823   Na_2O on the partial melting of spinel lherzolite in the system CaO–MgO–Al_2O_3–

824    $SiO_2 \pm H_2O \pm CO_2 \pm Na_2O$ at 1·1 GPa. Journal of Petrology, 47, 409-434.

825

826   Lukács, R., Czuppon, Gy., Harangi, Sz., Szabó, Cs., Ntaflos, T., and Koller, F. (2002) Silicate

827   melt inclusions in ignimbrites, Bükkalja Volcanic Field, Northern Hungary – texture and

828   geochemistry. Acta Geologica Hungarica, 45, 341–358.

829

830   Lukács, R., Harangi, Sz., Ntaflos, T., and Mason, P.R.D. (2005) Silicate melt inclusions in the

831   phenocrysts of the Szomolya Ignimbrite, Bükkalja Volcanic Field (Northern Hungary):

832   implications for the magma chamber processes. Chemical Geology, 223, 46–67.

833

834   Lukács, R., Harangi, S., Ntaflos, T., Koller, F., and Pécskay, Z. (2007) A Bükkalján megjelenő

835   felső riolittufaszint vizsgálati eredményei: a harsányi ignimbrit egység. (The characteristics of the

836   Upper Rhyolite Tuff Horizon in the Bükkalja Volcanic Field: The Harsány ignimbrite unit.)

837   Geological Bulletin of Hungary, 137, 487–514. (in Hungarian with English abstract)

838

839   Lukács, R., Harangi, Sz., Mason, P.R.D., and Ntaflos, T. (2009) Bimodal pumice populations in

840   the 13.5 Ma Harsány ignimbrite, Bükkalja Volcanic Field, Northern Hungary: syn-eruptive

841   mingling of distinct rhyolitic magma batches? Central European Geology, 52, 51–72.

842

843   Lukács, R., Harangi, Sz., Radócz, Gy., Kádár, M., Pécskay, Z., and Ntaflos, T. (2010) A

844   Nyékládháza-1, Miskolc-7 és Miskolc-8 sz. fúrások miocén vulkáni kőzetei és párhuzamosításuk

36

845   a Bükkalja vulkáni képződményeivel. (The Miocene pyroclastic rocks of the boreholes Miskolc–

846   7, Miskolc–8 and Nyékládháza–1 and their correlation with the ignimbrites of Bükkalja.)

847   Geological Bulletin of Hungary, 140, 31–48. (in Hungarian with English abstract)

848

849   Matthews, N.E., Pyle, D.M., Smith, V.C., Wilson, C.J.N., Huber, C., and van Hinsberg, V.

850   (2012) Quartz zoning and the pre-eruptive evolution of the ~340-ka Whakamaru magma systems,

851   New Zealand. Contributions to Mineralogy and Petrology, 163, 87-107.

852   doi: 10.1007/s00410-011-0660-1

853

854   Márton, E. (1990) Paleomagnetic studies on the Miocene volcanic horizons at the southern

855   margin of the Bükk Mts. Annual Report of the Eotvos Lorand Geophysical Institute, 1, 211–217.

856

857   Márton, E., and Pécskay, Z. (1998) Complex evaluation of paleomagnetic and K/Ar isotope data

858   of the Miocene ignimbritic volcanics in the Bükk Foreland, Hungary. Acta Geologica Hungarica,

859   41, 467–476.

860

861   Márton, E., Márton, P., and Zelenka, T. (2007) Paleomagnetic correlation of Miocene

862   pyroclastics of the Bükk Mts and their forelands. Central European Geology, 50, 47–57.

863

864   Mavrogenes, J.A., and Bodnar, R.J. (1994) Hydrogen movement into and out of fluid inclusions

865   in quartz: experimental evidence and geologic implications. Geochimica and Cosmochimica

866   Acta, 58, 141–148.

867

868   McClelland, E.A., and Druitt, T.H. (1989) Paleomagnetic estimates of emplacement temperatures

869   of pyroclastic deposits on Santorini, Greece. Bulletin of Volcanology, 51, 16–27.

870

871   McClelland, E., Wilson, C.J.N., and Bardot, L. (2004) Palaeotemperature determinations for the

872   1.8-ka Taupo ignimbrite, New Zealand, and implications for the emplacement history of a high-

873   velocity pyroclastic flow. Bulletin of Volcanology, 66, 492–513.

874   doi:10.1007/s00445-003-0335-5

875

876   McPhie, J., Doyle, M., and Allen, R. (1993) Volcanic textures: a guide to interpretation of

877   textures in volcanic rocks. 198 p. National Library of Australia, Canberra.

878

879   Müller, A., and Koch-Müller, A. (2009) Hydrogen speciation and trace element concentrations of

880   igneous, hydrothermal and metamorphic quartz from Norway. Mineralogical Magazine, 73, 569–

881   583.

882

883   Müller, A., Kronz, A., and Breiter, A. (2002) Trace elements and growth patterns in quartz: a

884   fingerprint of the evolution of the subvolcanic Podlesí Granite System (Krušné hory Mts., Czech

885   Republic). Bulletin of the Czech Geological Survey, 77, 135–145.

886

887   Müller, A., Wiedenbeck, M., Van Den Kerkhof, A.M., Kronz, A., and Simon, K. (2003) Trace

888   elements in quartz – a combined electron microprobe, secondary ion mass spectrometry, laser-

889   ablation ICP-MS, and cathodoluminescence study. European Journal of Mineralogy, 15, 747–

890   763.

891

892 Pécskay, Z., Lexa, J., Szakács, A., Seghedi, I., Balogh, K., Konečný, V., Zelenka, T., Kovacs, M.,

893 Póka, T., Fülöp, A., Márton, E., Panaiotu, C., and Cvetković, V. (2006) Geochronology of

894 Neogene magmatism in the Carpathian arc and intra-Carpathian area: a review. Geologica

895 Carpathica, 57, 511–530.

896

897 Pelikán, P. (2005) Explanatory Book to the Geological Map of the Bükk Mountains (1:50 000).

898 251 p. Geological Institute of Hungary, Budapest.

899

900 Peppard, B.T., Steele, I.M., Davis, A.M., Wallace, P.J., and Anderson, A.T. (2001) Zoned quartz

901 phenocrysts from the rhyolitic Bishop Tuff. American Mineralogist, 86, 1034–1052.

902

903 Riehle, J.R. (1973) Calculated compaction profiles of rhyolitic ash flow tuffs. Bulletin of the

904 Geological Society of America, 84, 2193–2216.

905

906 Riehle, J.R., Miller, T.F., and Bailey, R.A. (1995) Cooling, degassing, and compaction of

907 rhyolitic ash flow tuffs: a computational model. Bulletin of Volcanology, 57, 319–336.

908

909 Sambridge, M., FitzGerald, J., Kovács, I., O'Neill, H.St.C., and Hermann, J. (2008) Quantitative

910 IR spectroscopy with unpolarized light, Part I: Mathematical development. American

911 Mineralogist, 93, 751–764.

912

913   Severs, M.J., Azbej, T., Thomas, J.B., Mandeville, C.W., and Bodnar, R.J. (2007) Experimental

914   determination of H_2O loss from melt inclusions during laboratory heating: evidence from Raman

915   spectroscopy. Chemical Geology, 237, 358–371.

916

917   Shane, P., Smith, V.C., and Nairn, I. (2008) Millennial timescale resolution of rhyolite magma

918   recharge at Tarawere volcano: insights from quartz chemistry and melt inclusions.

919   Contribution Mineralogy and Petrology, 156, 397–411.

920

921   Skirius, C.M., Peterson, J.W., and Anderson, A.T. Jr. (1990) Homogenizing rhyolitic glass

922   inclusions from the Bishop Tuff. American Mineralogist, 75, 1381– 1398.

923

924   Stalder, R., and Konzett, J. (2012) OH defects in quartz in the system quartz–albite–water and

925   granite–water between 5 and 25 kbar. Physics and Chemistry of Minerals, 39, 817–827.

926   doi: 10.1007/s00269-012-0537-5

927

928   Stalder, R., and Neuser, D.R. (2013) OH-defects in detrital quartz grains: Potential for application

929   as tool for provenance analysis and overview over crustal average. Sedimentary Geology, 294,

930   118–126.

931   doi: http://dx.doi.org/10.1016/j.sedgeo.2013.05.013

932

933   Stenina, N.G. (2004) Water-related defects in quartz. Bulletin of Geosciences, 79, 251–268.

934

935   Szabó, Cs., Harangi, S., and Csontos, L. (1992) Review of Neogene and Quarternary volcanism

936   of the Carpathian-Pannonian region. Tectonophysics, 208, 243–256.

937

938   Szakács, A., Márton, E., Póka, T., Zelenka, T., Pécskay, Z., and Seghedi, I. (1998) Miocene

939   acidic explosive volcanism in the Bükk Foreland, Hungary: Identifying eruptive sequences and

940   searching for source locations. Acta Geologica Hungarica, 41, 413–435.

941

942   Thomas, S-M., Koch-Müller, M., Reichart, P., Rhede, D., Thomas, R., and Wirth, R. (2009) IR

943   calibrations for water determination in olivine, r-GeO$_2$ and SiO$_2$ polymorphs. Physics and

944   Chemistry of Minerals, 36, 489–509.

945   doi: 10.1007/s00269-009-0295-1.

946

947   Varga, Gy. (1981) New data to the knowledge of welded tuff formations and ignimbrites. Annual

948   report of the Hungarian Geological Institute from 1979, 499-509. (in Hungarian with English

949   abstract)

950

951   Wallace, P.J., Anderson, A.T., Jr., and Davis, A.M. (1999) Gradients in H2O, CO2, and exsolved

952   gas in a large-volume silicic magma system. Journal of Geophysical Research: Solid Earth, 104,

953   20097–20122.

954   doi: 10.1029/1999JB900207.

955

956   Wallace, P.,·Dufek, J.,·Anderson, A.T, and Zhang, Y. (2003) Cooling rates of Plinian-fall and

957   pyroclastic-flow deposits in the Bishop Tuff: inferences from water speciation in quartz-hosted

958   glass inclusions. Bulletin of Volcanology, 65, 105–123.

41

959

960   Wark, D.A., and Watson, E.B. (2006) TitaniQ: a titanium-in-quartz geothermometer.

961   Contribution to Mineralogy and Petrology, 152, 743–754.

962   doi 10.1007/s00410-006-0132-1

963

964   Wark, D.A., Hildreth, W., Spear, F.S., Cherniak, D.J., and Watson, E.B. (2007) Pre-eruption

965   recharge of the Bishop magma system. Geology, 35, 235-238.

966

967   Weis, F.A., Skogby, H., Troll, V.R., Deegan, F.M., and Dahren, B. (2015) Magmatic water

968   contents determined through clinopyroxene: Examples from the Western Canary Islands, Spain.

969   Geochemistry, Geophysics, Geosystems, 16, 2127–2146.

970

971   Weis, F.A., Stalder, R., and Skogby, H. (2016) Experimental hydration of natural volcanic

972   clinopyroxene phenocrysts under hydrothermal pressures (0.5–3 kbar). American Mineralogist,

973   101, 2233–2247.

974

975   Yagi K. (1966) Experimental study on pumice and obsidian. Bulletin of Volcanology, 29, 559–

976   572.

977

978   Zanella, E., Gurioli, L., Lanza, R., Sulpizio, R., and Bontempi, M. (2008) Deposition temperature

979   of the AD 472 Pollena pyroclastic density current deposits, Somma-Vesuvius, Italy, Bulletin of

980   Volcanology, 70, 1237–1248.

981

982

Figure captions

984   **Figure 1**. The location of the Bükk Foreland Volcanic Area (**a**) with Eger and Bogács sampling

985   localities (**b**). (**a**) The location of the Bükkalja Volcanic Field in the Carpathian-Pannonian

986   Region. The map was modified after Kovács et al. (2007). 1 - Middle Miocene- subrecent

987   volcanic rocks (exposed/subcrop); 2 - Early Miocene igneous rocks (exposed/subcrop); 3 -

988   Paleogene igneous rocks (exposed/subcrop); 4 - Main faults (exposed/subcrop); 5 - European

989   Foreland; 6 - Alcapa Units; 7 - Alpine-Carpathian Foredeep; 8 - Tisza-Dacia, Serbo-Macedonian

990   Units; 9 - Alpine-Carpathian Flysch Belt; 10 - Southern Alpine, Dinaric, Adriatic Platform Units;

991   11 - Mesozoic mélange and ophiolites; 12 - Bosnian Flysch

992   (**b**) The Bükk Foreland Volcanic Area with Eger and Bogács sampling localities. 1 - Lower, 2 -

993   Middle, 3 - Upper Ignimbrites. Other colors refer to Mesozoic and Cenozoic sedimentary

994   formations. See text for detailed volcanology.

995

996   **Figure 2.** Lithology of the investigated ignimbrites with sample locations and baseline corrected

997   average IR spectra. At Eger (**a**) the succession starts with a 0.2 m thick, well-sorted Plinian fall

998   deposit. Above, firstly a 0.3 m thick, cross-bedded fine tuff and then a ~30 m thick massive lapilli

999   tuff was deposited. At Bogács (**b**), except the lowermost 0.2 m thick basal contact the ignimbrite

1000   show increasing slightly welded character upwards. At both sites the uppermost part of the

1001   ignimbrites are recent erosional surfaces coated by soil. Between 3000 and 3550 cm^{-1} the main

1002   absorbance features are the Al-OH-related sharp bands at 3378, 3430, 3315 cm^{-1} which show

1003   clear decreasing absorbances as a function of height above the base. Above each spectrum, the

43

1004   number of analyzed phenocryst fragments (N) and the hydroxyl defect concentrations are also

1005   indicated. The lowering of the initial hydroxyl defect content is more gradual at Eger and more

1006   abrupt at Bogács in accordance with their different degree of welding.

1007

1008   **Figure 3.** The polarized and unpolarized absorbance indicatrices of Al-related hydroxyl defects

1009   in quartz with formulas for calculating polarized and unpolarized absorbances. (**a**) The ideal

1010   crystal form of quartz with principal crystallographic axes (*a, b, c*). (**b**) The polarized absorbance

1011   indicatrix of Al-related hydroxyl defect in quartz, which shows strong anisotropy. While the

1012   principal absorbances in the isotropic section are equal ($A_a^{pol} = A_b^{pol}$), the third principal

1013   absorbance which is parallel to *c* is zero ($A_c^{pol} = 0$). If the polarized light travels perpendicular to

1014   *c* (**c**) the polarized absorbance ranging between 0 and a maximum value as the orientation of the

1015   electric vector (**E**) varies with respect to A_a^{pol}. If the polarized light travels parallel to *c* (**d**), the

1016   polarized absorbance is maximal, regardless the direction of E.

1017   The polarized absorbance indicatrix can be converted to an unpolarized one assuming, that in

1018   each indicatrix section $A^{unpol} = 1/2(A_{max}^{pol} + A_{min}^{pol})$, where A^{unpol} is the unpolarized absorbance;

1019 A_{max}^{pol} and A_{min}^{pol} are the maximum and minimum polarized absorbances in a given indicatrix

1020   section (**e**). The unpolarized absorbance is equal to the length of the vector between the centroid

1021   and the surface of the absorbance indicatrix for any arbitrary directions of the incoming radiation.

1022   If the unpolarized radiation travels perpendicular to *c* (**f**) the unpolarized absorbance will be only

1023   the half of the polarized absorbances (A_a^{pol}, A_b^{pol}) in the isotropic section. If the unpolarized

1024   radiation travels parallel to *c* (**g**) the unpolarized absorbance is the same as the polarized

44

1025   absorbances in the isotropic section of the polarized absorbance indicatrix ($A_c^{\,unpol} = A_b^{\,pol} =$

1026 $A_a^{\,pol}$).

1027

1028   **Figure 4**. Representative quartz phenocrysts from the investigated samples. Big melt and fluid

1029   inclusions are abundant at the lowermost samples (E-1, BG-1). In samples from higher levels

1030   above the base melt and fluid inclusions are smaller and generally rarer. Black bars are 500

1031   micrometers in length.

1032

1033   **Figure 5.** Measured and modelled decrease of hydroxyl defect concentrations within quartz

1034   phenocrysts as a function of height above the base at Eger (**a**) and Bogács (**b**). Thickness is

1035   assumed to be 40 m in all model runs. The duration of all runs were 8 days. After 8 days the

1036   whole deposits cooled below 100°C, thus D became $<1.2 \times 10^{-17}$, consequently the dehydration

1037   was negligible. Initial temperatures are marked by different colours. C_i/C_0 refers to the ratio of

1038   initial and final amount of structural hydroxyl expressed in percents. d_{av} is the average crystal

1039   diameter that is used in modelling for a particular height above the base.

1040

1041   **Figure 6**. Representative concentration of trace elements and hydroxyl defects along transects in

1042   two phenocryst fragments from E-3 and BG-4 samples. Hydroxyl defect concentration shows

1043   very low and homogeneous concentrations. In contrast, for other trace elements their

1044   concentrations and variations are generally higher with two orders of magnitude.

1045

1046   **Table 1**. Main characteristics of the investigated localities and quartz phenocrysts. N - number of

1047   analyzed phenocryst fragments by Micro-FTIR spectroscopy; Fp - feldspars; Q - quartz; Bt -

1048   biotite; Opx - orthopyroxene; d_{av} – average grain diameter; n.o. - not observed

1049

1050   **Table 2**. The measured maximum, minimum and average unpolarized absorbances and the

1051   calculated principal polarized absorbances for each sample suite. The principal polarized

1052   absorbances were calculated using Equations 2 (see also Equations 70 in Sambridge et al. 2008).

1053   N - number of analyzed phenocryst fragments; Out - number of outliers, which were excluded

1054   from the calculation of principal polarized absorbances; A_{max}^{unpol}, A_{min}^{unpol}, A_{avg}^{unpol} - measured

1055   maximum, minimum and average unpolarized absorbances; A_a^{pol}, A_b^{pol}, A_c^{pol} - calculated

1056   principal polarized absorbances. Values in italic and marked with * symbol for E-3 and BG-2

1057   were calculated by omitting the outlier values.
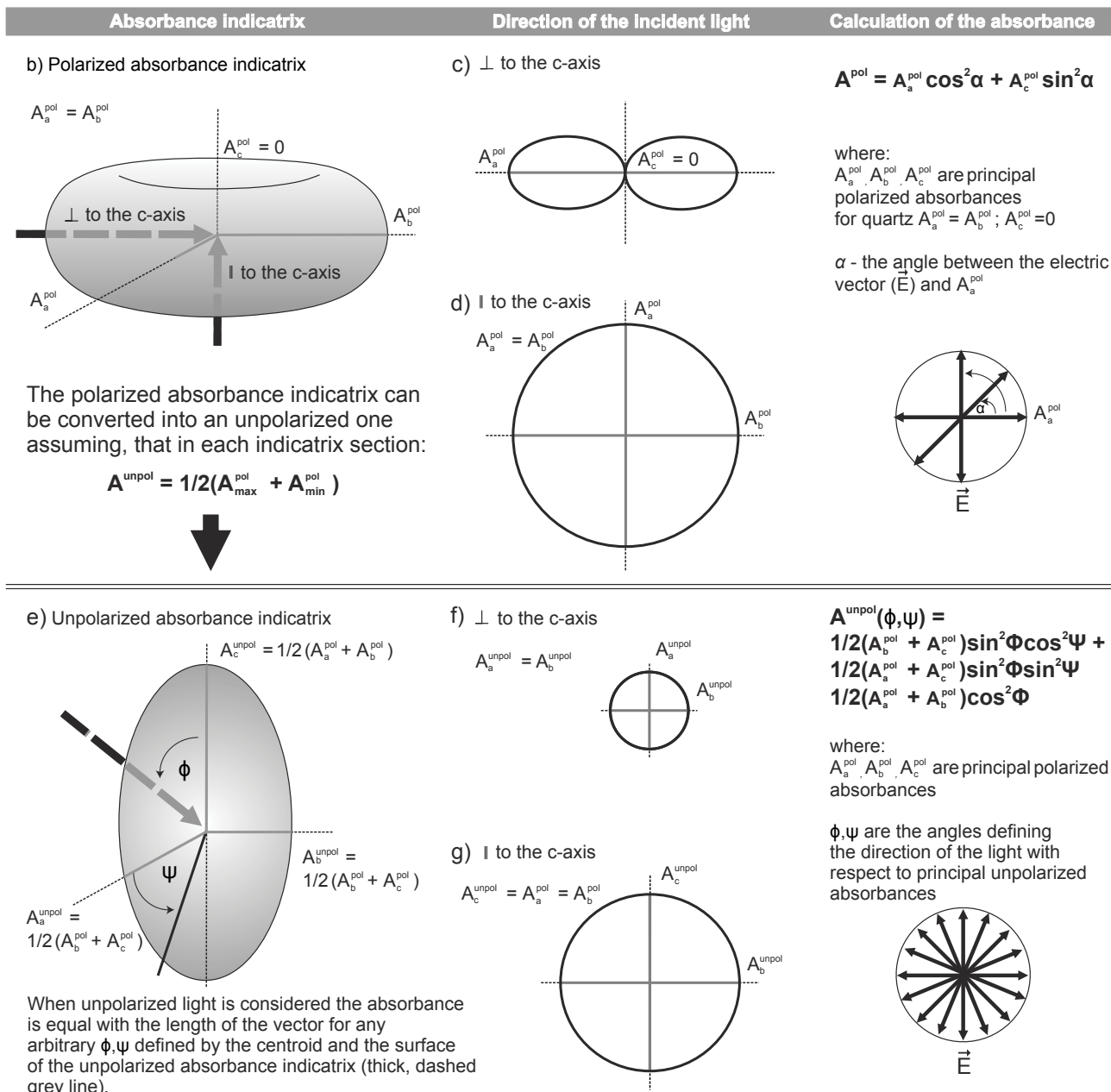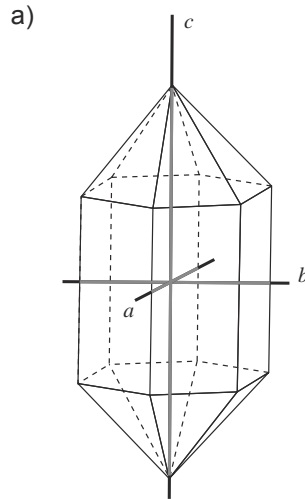
1058

Figure 1
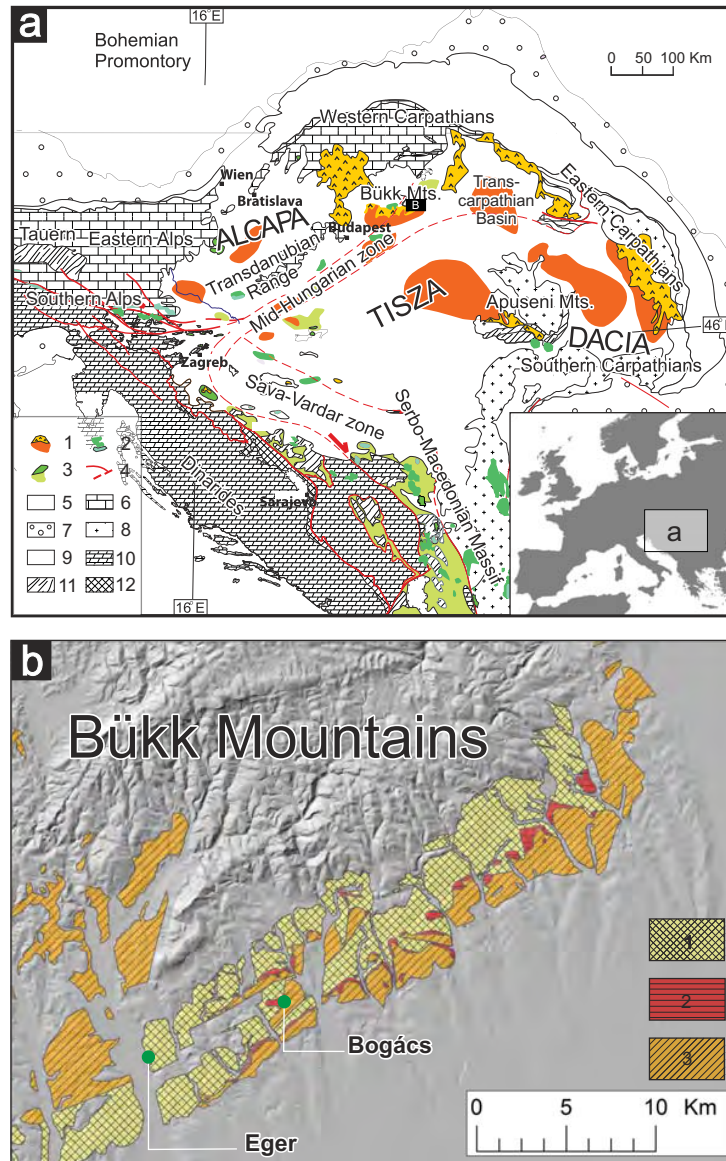
Figure 2
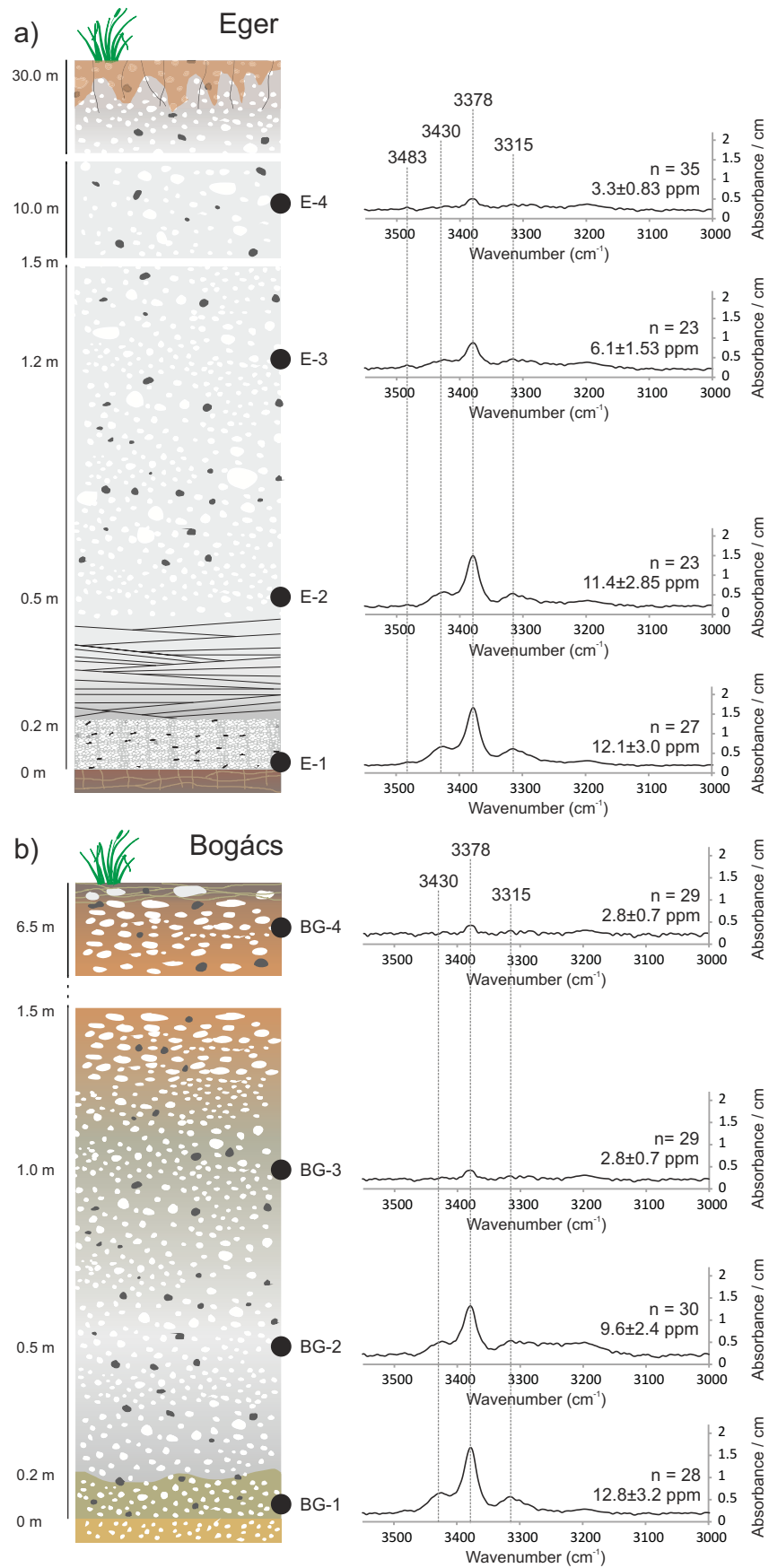
Figure 3

Figure 4
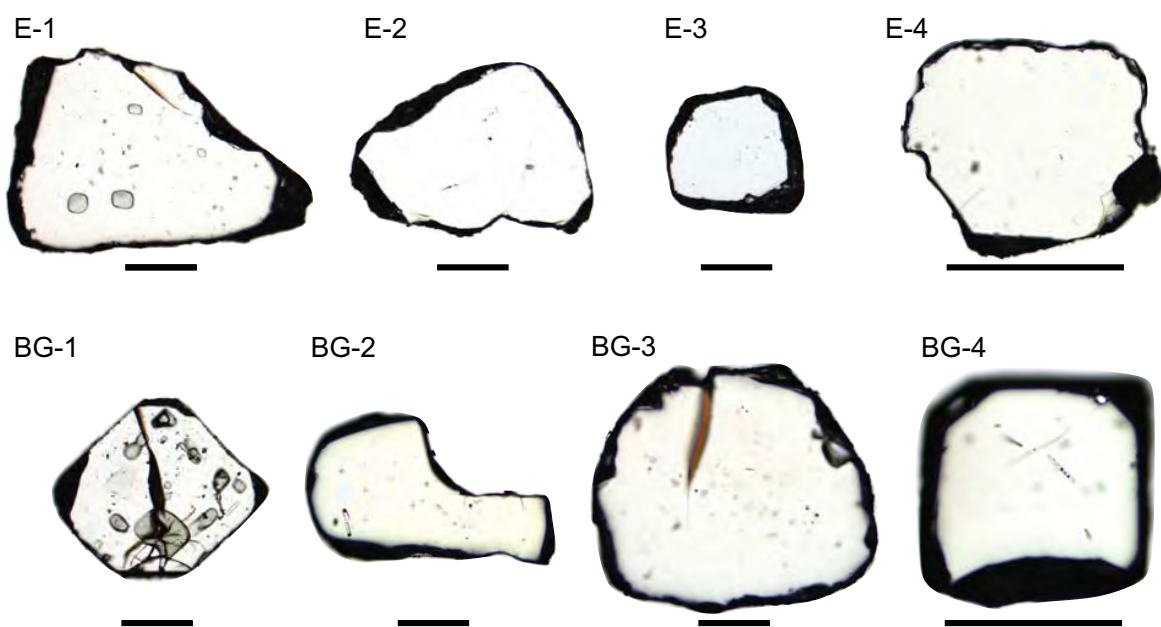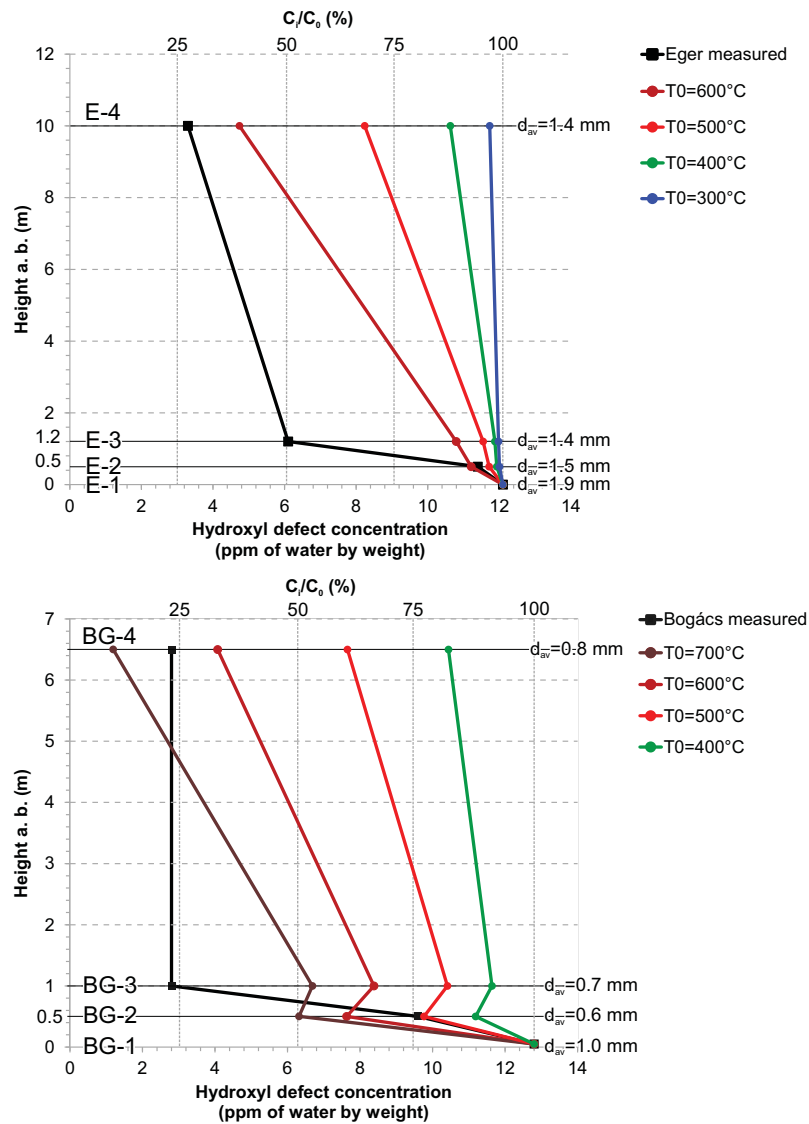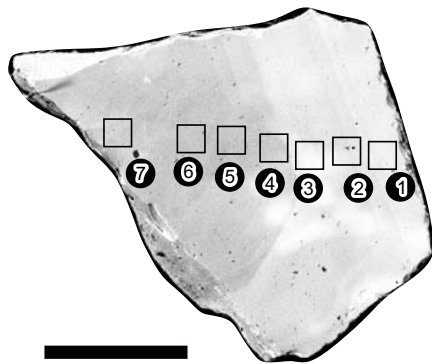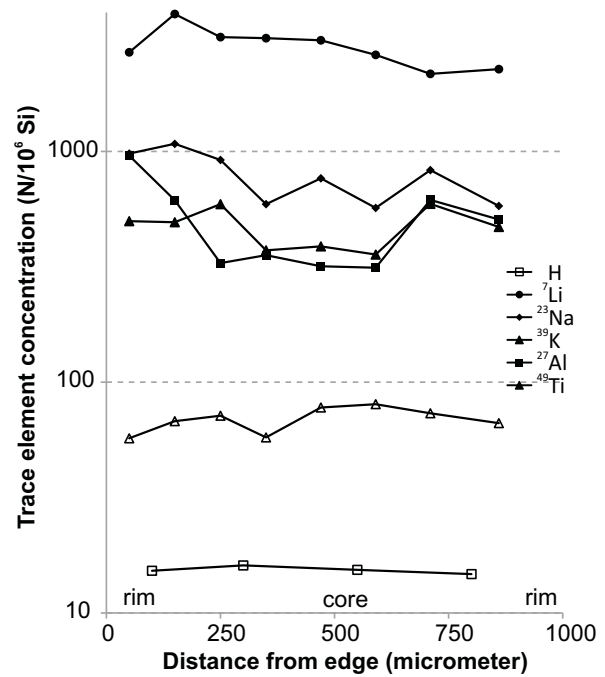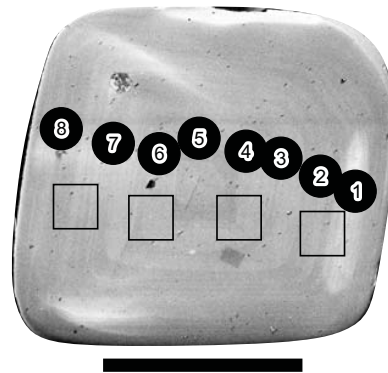
E-1

E-2

E-3
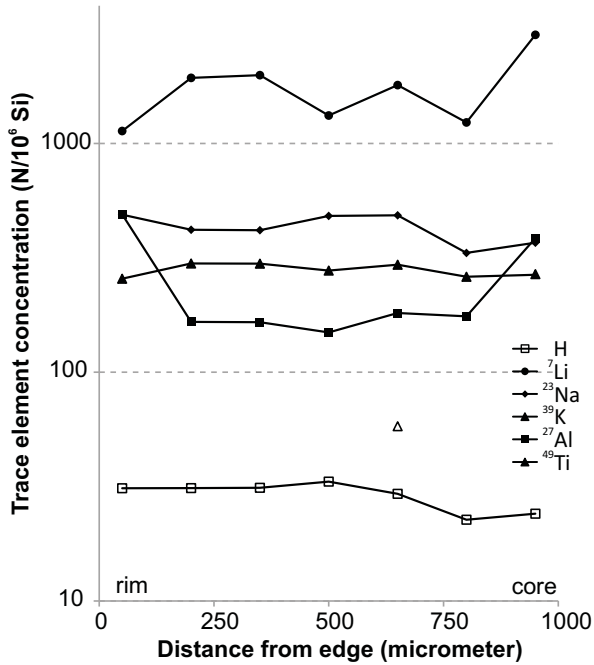
E-4

BG-1

BG-2

BG-3

BG-4

Fig. 5

Figure 6

Table 1. Main characteristics of the investigated localities and quartz phenocrysts.

					Outcrop						Quartz crystals				
Locality	N (dec. deg.)	E (dec. deg.)	Sample	Height a. b. (m)	Phenocrysts	Source	Max d. (mm)	d_{av} (mm)	Appearance	Resorption	Inclusions	N	Average hydroxyl defect conc. (ppm H_2O by wt.)	Average hydroxyl defect conc. (H / 10^6 Si)
Eger	47.885	20.404	E-4	10.0	Fp>Q>Bt	from pumices and matrix	3	1.4	fragments of euhedral, bipiramidal phenocrysts; fractures are abundant	n.o.	rounded and hourglass melt inclusions are abundant just above the lower contact, however melt inclusions are more and more rare upward the succesion	35	3.3	22.0
			E-3	1.2			3	1.4				23	6.1	40.6
			E-2	0.5			3	1.5				23	11.4	75.9
			E-1	0.0		individual crystal fragments	4	1.9				27	12.1	80.6
Bogács	47.923	20.508	BG-4	6.5	Fp>Bt>Q>Opx; the amount of Q is decreasing upward; the amount of Opx is increasing upward	from pumices and matrix	1	0.8	euhedral, bipiramidal phenocrysts; fragments are rare	on the largest crystals	irregularly shaped melt inclusions are abundant just above the lower contact, however melt inclusions are more and more rare upward the succesion	29	2.8	18.6
			BG-3	1.0			1	0.7				29	2.8	18.6
			BG-2	0.5			1	0.6				30	9.6	63.9
			BG-1	0.1			2	1				28	12.8	85.2

Table 2. The measured maximum, minimum and average unpolarized absorbances and the calculated principal polarized absorbances for each sample suite.

Sample	N	Out	Measured unpolarized absorbances			Calculated principal polarized absorbances			
			A_{avg}^{unpol} (cm^{-2})	A_{min}^{unpol} (cm^{-2})	A_{max}^{unpol} (cm^{-2})	A_a^{pol} (cm^{-2})	A_b^{pol} (cm^{-2})	A_c^{pol} (cm^{-2})	$(A_b^{pol} + A_c^{pol}/2)$ (cm^{-2})
E-4	35	-	14.55	9.14	23.09	-2.53	20.81	25.38	23.09
E-3*	22	-	26.96	18.37	45.30	-9.71	46.45	44.15	45.30
E-3	23	1	28.31	18.37	57.86	-30.81	67.54	48.18	57.86
E-2	23	-	53.78	42.22	76.31	8.71	75.72	76.89	76.31
E-1	27	-	58.17	42.87	77.88	18.74	67.01	88.75	77.88
BG-4	29	-	13.51	10.19	19.35	1.82	18.55	20.14	19.35
BG-3	29	-	13.48	10.83	21.61	-2.78	24.45	18.78	21.61
BG-2*	28	-	47.65	34.36	67.46	8.05	60.68	74.23	67.46
BG-2	30	2	45.25	11.46	67.46	0.83	22.09	112.83	67.46
BG-1	28	-	58.91	44.96	66.02	44.69	45.23	86.81	66.02